Ground-Motion Modeling Using MyShake Smartphone Peak Acceleration Data

Savvas Marcou*[1], Richard M. Allen[1], Norman A. Abrahamson[2], and Chih-Hsuan Sung[2]

ABSTRACT

In the field of ground-motion modeling, the availability of densely sampled ground-motion data is becoming key to mapping repeatable source, path, and site effects to enable ground-motion models (GMMs) to more accurately predict shaking from future earthquakes. This is particularly important because the field is moving toward nonergodic GMMs with spatially variable coefficients. To achieve the level of sampling required, the addition of non-instrumental data collected at very high spatial resolution, like felt intensity data or smartphone data, could prove essential. The predictive power of this nontraditional data for free-field ground motion needs to be tested before these data are used. In this work, we present a new database of over 1600 ground-shaking waveforms collected between 2019 and 2023 by the MyShake smartphone app, which delivers earthquake early warning messages to users on the U.S. West Coast. We develop a GMM, MyShake GMM, for peak smartphone-recorded accelerations in $3 \leq M \leq 5.5$ earthquakes recorded at short (< 50 km) distances. We compare our model with free-field GMMs and show a similar geometric decay and a close match in predicted amplitudes for short-period spectral accelerations (SAs). We use residual correlation analysis to show that MyShake GMM residuals have a positive correlation with free-field residuals, with correlation coefficients of around 0.4 for peak ground acceleration, velocity, and short-period SA, similar to correlations previously reported between felt intensity and free-field data. This illustrates the potential that densely sampled smartphone ground-shaking data has in identifying repeatable free-field ground-motion effects for various ground-motion modeling applications. These could potentially include highly location-specific assessments of site response, ground-motion interpolation schemes like ShakeMap, or validating outputs from nonergodic, spatially variable coefficient GMMs.

KEY POINTS

- Smartphone waveforms provide complementary coverage to free-field ground-motion data.
- A predictive model is developed for peak smartphone acceleration.
- Systematic effects mapped by smartphone data show predictive power for free-field ground motion.

Supplemental Material

INTRODUCTION

The prediction of earthquake ground motion for a site for a specific earthquake scenario, given a magnitude, source-to-site distance, and site condition, is a key issue in the field of seismic hazard analysis. At present, seismic hazard models like the U.S. National Seismic Hazard Model rely on ground-motion models (GMMs) to convert earthquake rate models into predictions of ground motion over the entire domain of interest (Moschetti *et al.*, 2024; Petersen *et al.*, 2024). The development of GMMs relies on the availability of large databases of ground-motion records that sample the entire ranges of earthquake magnitudes, distances, and site conditions well enough to allow for the constraining of coefficients. Traditionally, GMMs were developed under the ergodic assumption (e.g., Abrahamson and Silva, 1997), whereby it was assumed that similar tectonic regions behaved similarly (e.g., attenuation for all active crustal regions globally behaved the same) in terms of magnitude scaling and the distance attenuation of ground motion. This allowed model developers to use data from other regions to improve data coverage in a key region of interest (e.g., data from Taiwan used to inform models for California). More recently, the field of GMMs has been gradually evolving to remove the ergodic assumption. First, partially nonergodic GMMs were developed that explicitly

---

1. Berkeley Seismological Laboratory, University of California, Berkeley, Berkeley, California, U.S.A., https://orcid.org/0000-0003-3961-773X (SM); https://orcid.org/0000-0003-4293-9772 (RMA); 2. Department of Civil and Environmental Engineering, University of California, Berkeley, Berkeley, California, U.S.A., https://orcid.org/0000-0001-7900-6023 (NAA); https://orcid.org/0000-0001-7606-0366 (C-HS)

*Corresponding author: savvas.marcou@berkeley.edu

Cite this article as Marcou, S., R. M. Allen, N. A. Abrahamson, and C.-H. Sung (2024). Ground-Motion Modeling Using MyShake Smartphone Peak Acceleration Data, *Bull. Seismol. Soc. Am.* **115**, 86–105, doi: 10.1785/0120240209

accounted for the repeatable site effects by removing the site-to-site variability from the aleatory variability and including the estimate of the site-specific site term as part of the median (McCann and Addo, 2012). This approach was called single-station sigma. Next, differences in the distance attenuation, site scaling, and the constant term for broad regions were included in the GMMs. The GMMs developed in the Next Generation Attenuation-West2 (NGA-West2) project (Bozorgnia *et al.*, 2014) are an example of regionalized GMMs. The current state-of-the-art lies with fully nonergodic models that model systematic source, path, and site effects on the ground motion by allowing the coefficients of the GMM to vary spatially (Landwehr *et al.*, 2016; Lavrentiadis *et al.*, 2022). This can be thought of as a regionalized GMM with small regions of dimensions represented by the spatial correlation lengths of the coefficients. For sites located far away from data, the median nonergodic model falls back to the ergodic backbone GMM, but with large epistemic uncertainty in the nonergodic terms. The estimation of variance and correlation lengths of the nonergodic terms requires dense data coverage. There is an increasing number of studies trying to use spatially dense simulated records of earthquakes to increase the spatial coverage (e.g., Sung *et al.*, 2023), but these simulations depend on having a correct earth structure and earthquake source model, which are assumptions that are hard to verify.

New nonergodic models can benefit from dense crowdsourced data for either estimation or validation of nonergodic terms. Felt intensity observations from the U.S. Geological Survey (USGS) "Did You Feel It?" (DYFI; Quitoriano and Wald, 2020) generally track trends observed in instrumental free-field ground-motion measurements (Atkinson and Wald, 2007) and have been used to conduct various ground-motion studies at high spatial resolution in which seismic sensor data are sparse or nonexistent (e.g., Van Noten *et al.*, 2017; Rosset *et al.*, 2022). The MyShake smartphone platform provides another alternative dataset for dense spatial coverage of ground motion. MyShake is a free smartphone application available for both iOS and Android devices with about 3 million users globally. The app currently has about 2 million users on the U.S. West Coast alone, where it serves as one of the principal delivery mechanisms for earthquake early warning (EEW) alerts issued by the USGS ShakeAlert (EEW) system (Given *et al.*, 2018; Strauss *et al.*, 2020; Patel and Allen, 2022). MyShake data provide a key means of assessing warning times to users (Patel and Allen, 2022). However, MyShake was originally conceived as a global crowdsourcing platform for earthquake data (Kong, Allen, Schreier, and Kwon, 2016). MyShake currently provides a simple thumbnail-based survey to enable the user to submit felt reports that perform comparably with DYFI data in capturing felt intensity (Kong *et al.*, 2023). It also collects triggered acceleration waveforms using the onboard smartphone accelerometer.

The triggered waveforms collected by MyShake have been used recently to successfully measure building structural response to earthquake shaking (Patel *et al.*, 2023), but given their dense spatial sampling, they could also illuminate fine-scale details of ground motion (Kong *et al.*, 2018, 2019; Patel and Allen, 2022). Smartphone acceleration data from MyShake and other smartphone data collection efforts like the Earthquake Network (Finazzi, 2016, 2020) generally show expected trends, like peak accelerations that increase with magnitude and decrease with distance (Kong, Allen, and Schreier, 2016; Finazzi *et al.*, 2024). Such trends have already been leveraged for the development of smartphone-based magnitude scaling laws for EEW applications (Kong, Allen, Schreier, and Kwon, 2016; Finazzi *et al.*, 2024). However, a detailed study of how smartphone accelerations compare to free-field records as well as the predictive power smartphone data hold for estimating free-field ground motion remains lacking. Patel and Allen (2022) used smartphone waveforms from five events in California to study the relationship between smartphone-recorded peak acceleration and peak ground acceleration (PGA) in the free field. They found that MyShake smartphone waveforms record accelerations that were a median of 3.1 times higher than those recorded at free-field sites. This is an intriguing observation that merits further investigation before MyShake data can be used to study ground motion. Although there is a large factor between the smartphone PGA values and the free-field PGA values, the spatial distribution of the smartphone residuals may be correlated with the spatial distribution of the free-field PGA residuals, which would allow the smartphone data to help constrain or test the nonergodic models for free-field ground motions.

In this study, we compile an expanded smartphone waveform database, with a focus on the U.S. West Coast. We then analyze the differences between free-field and smartphone-recorded ground-motion intensity in a ground-motion framework, using GMMs. We develop a predictive GMM for MyShake smartphone-recorded peak acceleration and use it to investigate the correlation of repeatable effects captured by the MyShake and free-field intensity measures (IMs), using the residuals from GMMs. We show MyShake data have comparable predictive power to felt intensity data for free-field ground motion when it comes to short-period metrics. With this in mind, we discuss potential applications for the MyShake model and dataset in ground-motion modeling.

SMARTPHONE WAVEFORM DATABASE

To assess the utility of triggered smartphone acceleration waveforms for ground-motion modeling, we first assemble a database of smartphone records of ground shaking from cataloged earthquakes.

Waveform recording by MyShake devices is initiated via two alternative avenues. Waveform recording can be triggered via a trigger declared by an onboard instance of a short-term/long-term average (STA/LTA) triggering algorithm (Allen, 1978) and confirmed as earthquake-related via a shallow artificial neural network (ANN) classifier (Kong, Allen, Schreier, and Kwon, 2016). Alternatively, user devices are instructed to record in all instances in which the phone is found to be within the modified Mercalli intensity (MMI) II (defined by the MMI 1.5 computed radius) contour issued by the USGS ShakeAlert system and the ShakeAlert maximum magnitude estimate is $M \geq 3.5$ (Patel and Allen, 2022). This means that the system not only triggers waveform recordings in cases in which the ShakeAlert public alerting thresholds of MMI III and magnitude 4.5 (Kohler *et al.*, 2020) are met but also does so for smaller earthquakes with a large potential for providing waveform data. Five minutes of waveform data, 1 min before and 4 min after the trigger time, are collected on the phone and are transmitted to the MyShake backend servers when the device is connected to power and Wi-Fi (Patel and Allen, 2022). Three-component (vertical and two orthogonal horizontal components) waveforms are stored for analysis along with the device-provided location, phone elevation, and horizontal location uncertainty.

To build our smartphone ground-motion record database, we first search the MyShake waveform archive for any waveforms that were triggered within magnitude-dependent spatiotemporal windows (see Table S1, available in the supplemental material to this article) with respect to all earthquakes in the USGS Comprehensive Earthquake Catalog (ComCat; Guy *et al.*, 2015) at $M \geq 2.5$ for the period 1 January 2019–16 February 2023. Through this process, we associate a total of 18,943 individual records with 1675 earthquake events. Next, to ensure only waveforms with a convincing earthquake signal are used for analysis, we inspect all waveforms manually.

We inspect waveforms visually in a window from 1 s before the estimated *P*-wave arrival at the phone's location to 1.5 times the *S*-wave arrival time (using constant V_P and V_S of 6 and 3.5 km/s, respectively). We use the following criteria to admit waveforms for further analysis:

1. The waveform includes a signal at least 2 s before the estimated *S*-wave arrival.
2. There is a convincing earthquake signal with a clear peak.
3. There are no visible glitches, unnatural spikes, or cyclical, repeating signals.
4. There is no obvious clipping (due to phone sliding; Patel *et al.*, 2023).

All waveforms that pass visual inspection are trimmed to the signal window, restored to horizontal, and high-pass filtered at 0.5 Hz to eliminate any long-period drifts. We record MyShake peak acceleration as the maximum of the two as-recorded restored horizontal components. We also compute the geometric mean of the two horizontals. To produce our final database, which we call the MyShake ground-motion database (GMDB), only waveforms with a device-reported horizontal location accuracy of 35 m or better are admitted. Following this quality assurance procedure, we are left with 1619 waveforms (i.e., 8.5% of initial waveforms) from a total of 224 individual earthquake events. Locations of records and events are shown in Figure 1. 85% of MyShake GMDB records were triggered by receipt of an EEW message, with the remaining 15% of recordings triggered by the onboard STA/LTA + ANN triggering logic. Perhaps unsurprisingly, the vast majority (96%) of our waveforms are located in California and cluster strongly around large urban centers like the Los Angeles basin and the San Francisco Bay Area, where MyShake serves large numbers of users as part of the EEW alerting effort.

For the earthquakes in our final database with at least one smartphone record, we assemble an event information table using source information from the USGS ComCat. We collect the authoritative epicenter, depth, magnitude, focal mechanism, and finite-fault model (if available). In cases in which the events have a moment magnitude (M_w) available, it is preferred, whereas for those events without an M_w, we use the catalog preferred magnitude (usually local magnitude M_L, or duration magnitude M_D), following the practice used in the NGA-West2 database (Ancheta *et al.*, 2014). We also classify events as strike-slip, normal, reverse, or oblique, following the scheme described in García *et al.* (2012), using the faulting mechanisms provided by moment tensors (where available) or first-motion polarity focal mechanisms. Using the event information, we calculate hypocentral (R_{hyp}) and epicentral (R_{epi}) distances for all smartphone records, as well as rupture (R_{rup}) and Joyner–Boore (R_{JB}) distances for records, causative events of which have a finite-fault model available. For events without a finite-fault model, we assume $R_{rup} = R_{hyp}$ and $R_{JB} = R_{epi}$. We use the time-averaged shear-wave velocity in the top 30 m (V_{S30}) as a site parameter. We assign each record a value from the 2022 update of the Thompson *et al.* (2014) map-based V_{S30} model for California (for California records) or the USGS global V_{S30} mosaic (Heath *et al.*, 2020) via the nearest-neighbor interpolation.

The magnitude–distance distribution of our dataset against the NGA-West2 database is shown in Figure 2. In the 4 yr covered by our dataset, MyShake managed to collect one-tenth of the total number of records included in the NGA-West2 database, which covers almost 80 yr of records. We see that MyShake records overwhelmingly sample small and moderate magnitude (**M** 3.0–6.0) earthquakes at relatively short source-to-site distances. The smartphone database adds considerable data density at these short distances and small-to-moderate magnitude earthquakes. Few data points are added at $M \geq 5.5$, owing to MyShake GMDB's short temporal sampling of the earthquake record.

COMPARISON OF SMARTPHONE AND FREE-FIELD OBSERVATIONS

We next compare MyShake-recorded waveforms to free-field ground-motion records, extending the analysis that Patel and

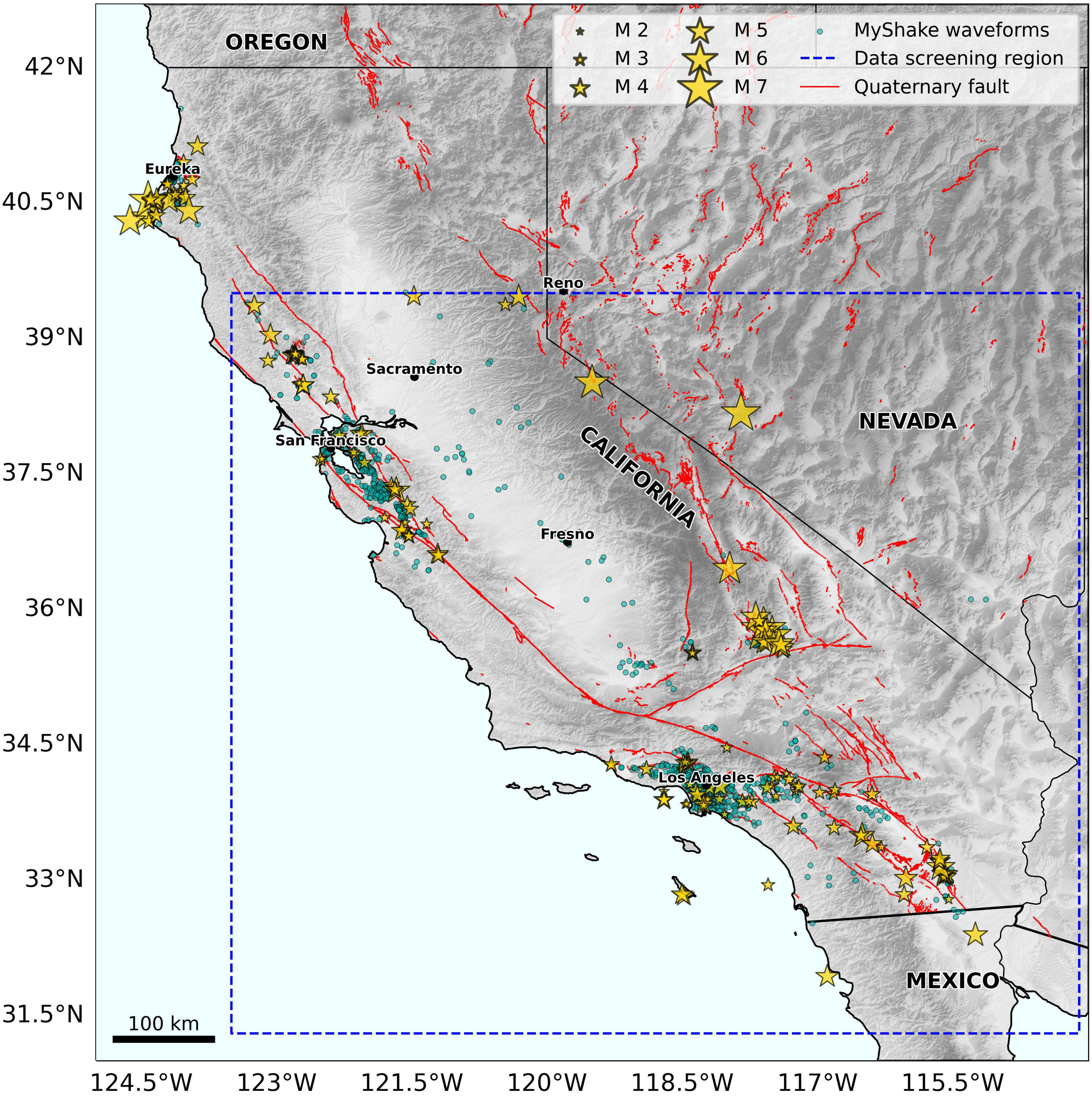

Figure 1. Events sampled by the MyShake database and locations of smartphone waveforms in California. 96% of the total 1619 records in the MyShake ground-motion database (GMDB) are located within the plotting area of this map and are plotted here. Events are plotted as stars scaled by magnitude. Waveform records are plotted as dots. We also plot faults active within the last 15 ky from the U.S. Geological Survey Quaternary Faults Database (U.S. Geological Survey and California Geological Survey, 2020) as red lines. The blue polygon indicates the area where events and records are considered for further ground-motion analysis in the Ground-Motion Modeling Methodology section. The color version of this figure is available only in the electronic edition.

Allen (2022) conducted on five California earthquakes. To perform this analysis, we cast both the free field and the smartphone records in ground-motion residual space (with respect to the NGA-West2 suite of active crustal GMMs), rather than a straight comparison to free-field observations, as was done by Patel and Allen (2022). We believe that using the NGA-West2 suite of active crustal GMMs should represent free-field ground motion well on average, given these were derived using the extensive NGA-West2 database and avoid any potential selection bias. Furthermore, viewing ground-motion datasets in residual space is a popular way of analyzing spatially variable systematic effects with respect to median models and studying

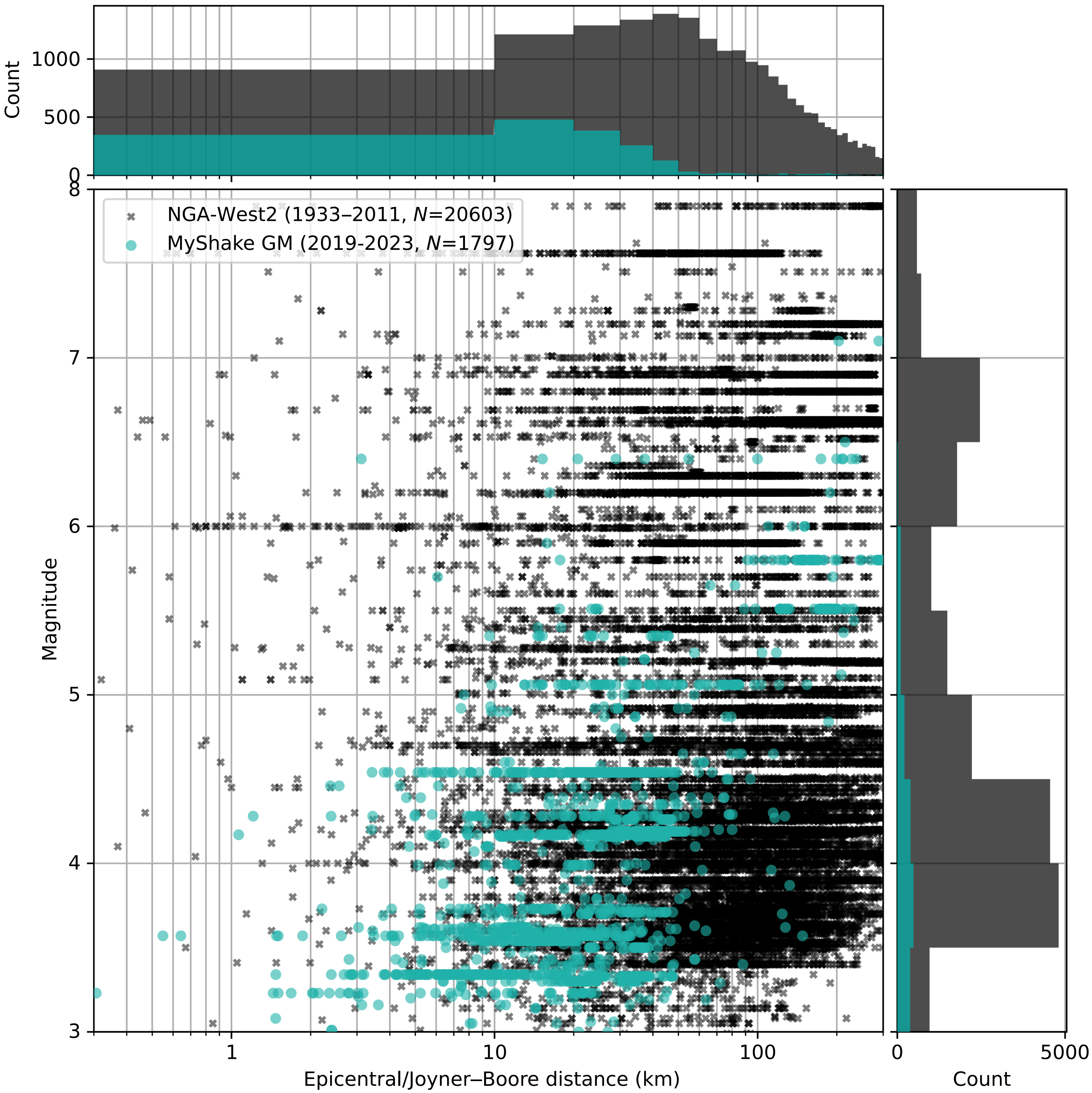

Figure 2. Magnitude–distance distribution of the MyShake GMDB against the Next Generation Attenuation-West2 (NGA-West2) database. Only data at $R_{JB} \leq 300$ km is shown. The color version of this figure is available only in the electronic edition.

potential correlations of systematic effects across different ground-motion metrics (e.g., Baker and Cornell, 2006; Carlton and Abrahamson, 2014).

To make a fair comparison, we limit the MyShake database to the active crustal region from which records were included in the NGA-West2 database (see Fig. 1), and for which the NGA-West2 suite of active crustal GMMs applies. For all earthquakes for which at least one smartphone record is available, we download all available free-field station observations used for computing the event ShakeMap from the USGS ComCat. We then compute median ground-motion amplitude predictions for all five ShakeMap output intensity metrics (PGA, peak ground velocity [PGV], and spectral acceleration [SA] at 0.3, 1.0, and 3.0 s) for all MyShake and free-field observation sites using a weighted average of the Abrahamson *et al.* (2014; hereafter, ASK14), Boore *et al.* (2014; hereafter, BSSA14), Campbell and Bozorgnia (2014; hereafter, CB14), and Chiou and Youngs (2014; hereafter, CY14) NGA-West2

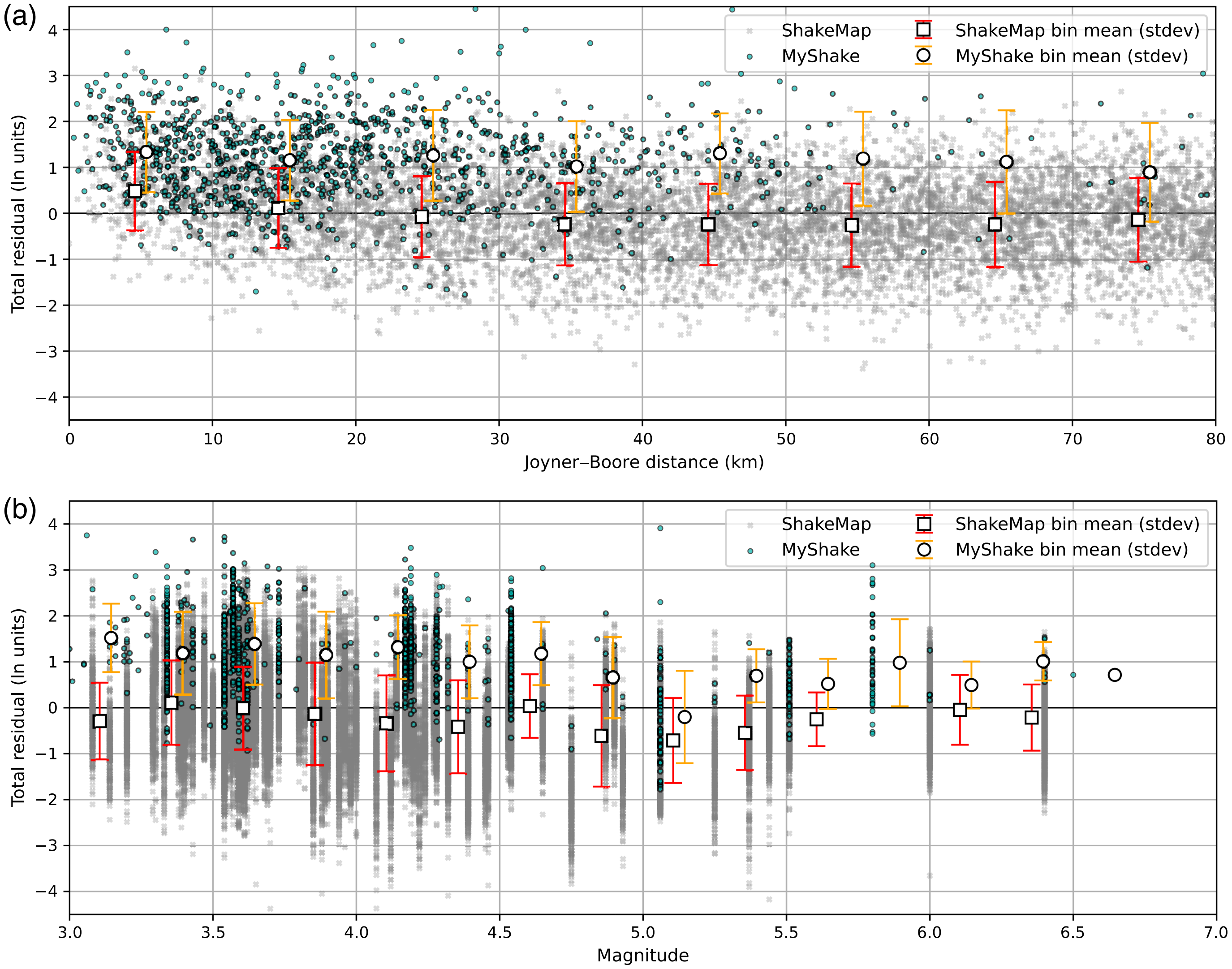

Figure 3. Comparison of total (δ_{ij}) peak ground acceleration (PGA) residuals (ln[osberved]–ln[predicted]) of MyShake (turquoise) and ShakeMap (gray) observations against an average prediction from an ensemble of NGA-West2 ground-motion models (GMMs), in natural log units, plotted against (a) Joyner–Boore distance and (b) magnitude. Individual observations are shown as dots. Filled symbols (dots for MyShake and squares for ShakeMap free-field data) indicate binned means and error bars indicate standard deviations. These are plotted with a slight offset for clarity. The color version of this figure is available only in the electronic edition.

GMMs. For events without a finite-fault model, we use the hypocentral distance as the input rupture distance and the hypocentral depth as the depth to the top of the rupture (Z_{TOR}). We evaluate GMM predictions for each site using the site V_{S30} but set the basin amplification terms to zero. ShakeMap observations are reported as the maximum of the two horizontal components, whereas GMM predictions are for the median rotation-dependent amplitude (RotD50); we therefore adjust the RotD50 GMM prediction accordingly using the ratios of Boore and Kishida (2016).

Finally, we form total ground-motion residuals (δ_{ij}) for all observations as

$$\delta_{ij} = \ln(Y_{ij}) - \ln(\mu(M_i, R_{ij}, V_{S30,j}, \ldots)), \qquad (1)$$

in which Y_{ij} is the observed ground-motion amplitude and $\mu(M_i, R_ij, V_{S30,j}, \ldots)$ is the GMM prediction for the ith earthquake observed at the jth site. In this formulation, overprediction by the GMM yields a negative residual, whereas underprediction yields a positive residual.

We plot the individual observations, as well as binned means, against magnitude and Joyner–Boore distance (R_{JB}) in Figure 3. It can be clearly seen that with respect to predicted PGA, the MyShake records are biased high, whereas the free-field records are mostly centered around zero, indicating the NGA-West2 GMMs are unbiased, as previously found by Chatterjee *et al.* (2022). The magnitude of the overprediction for the MyShake data varies with magnitude and distance. The sample mean of $\delta_{ij,\mathrm{PGA}}$ is 1.2 natural log units, or 3.7 times, even higher than the median factor of 3.1 reported by Patel and Allen (2022). When we subset the dataset to include only the events Patel and Allen (2022) considered, we are able to reproduce their results. When the same exercise is repeated for SA(0.3 s), we find a sample mean of 0.9 natural log units, or 2.4 times, with similar distance and magnitude trends. This is higher than what Patel and Allen (2022) report, but essentially confirms their conclusion that when attempting to model MyShake data using free-field GMMs, the closest match is achieved using short-period (0.1–0.3 s) SA as the target IM. This is in line with the fact that MyShake smartphone waveforms are recorded within buildings and therefore capture ground motion modified by the building's response, as well as any potential effects of nonstructural elements that hold the phones. Most waveforms in our database can be traced back to regions dominated by low-rise (1–3 story-tall) residential buildings, which are expected to have fundamental periods in the 0.1–0.5 s range (American Society of Civil Engineers, 2021).

It is clear from this analysis that forming MyShake ground-motion residuals with respect to free-field GMMs, for applications like ShakeMap or partially nonergodic ground-motion modeling, would result in biased residuals. A correction by simply subtracting a static bias would not be viable, given that the bias varies with magnitude and distance. We thus propose that MyShake smartphone acceleration observations should be treated as a distinct IM, rather than considered to sample free-field acceleration. We, therefore, proceed to derive a "ground-motion" model specifically for smartphone-recorded peak acceleration.

GROUND-MOTION MODELING METHODOLOGY

Data subsetting

To develop a predictive model for MyShake smartphone-recorded peak accelerations, we start by selecting a subset of our dataset, such that model coefficients are well constrained by the data. We also seek to enable meaningful comparisons with the NGA-West2 active crustal GMMs, which are generally applicable down to M 3.0 and at distances <300 km. As seen in Figure 2, there is a lack of MyShake data at distances >80 km. Furthermore, data are extremely sparse above M 6. For instance, the only records at 5.5< M <6.0 are waveforms at $R > 100$ km from the 2020 M 5.8 Lone Pine earthquake. We thus select only records with $0 \le R_{epi} \le 50$ km, recording events of $3.0 \le M \le 5.5$, that lie within the blue "Data Screening" box in Figure 1 and have depths ≤20 km.

The final dataset of selected records and events is described in Figure 4. Ninety-two events, sampled by a total of 942 records, are included in our final dataset. About 85% of events (78 events) have 10 waveforms or less, whereas 29% of events (27 events) have 3 waveforms or more (Fig. S2). The dataset is strongly dominated by data in the San Francisco Bay Area and the Los Angeles basin, which are major urban areas with a large MyShake user base. Figure 4c shows that the V_{S30} distribution of the selected records is dominated by records with a V_{S30} around the C/D National Earthquake Hazards Reduction Program (NEHRP) site class boundary (median of 316 m/s). Our V_{S30} distribution is very similar to the V_{S30} distribution sampled by global felt intensity reports in the USGS DYFI database used by Allen *et al.* (2012). This is not surprising, as both MyShake and felt intensity data overwhelmingly sample urban areas.

Functional forms and model fitting

To determine our predictive model for smartphone-recorded peak acceleration, we use simple functional forms for the source (magnitude) and path (geometric spreading) terms that are common in ground-motion modeling and are supported by the data. For instance, Figure 5 shows a clear decay of MyShake accelerations with distance. There is a dependence with magnitude that we capture with a linear magnitude scaling term. We do not see a magnitude saturation effect (a "bunching" of points from larger magnitude events) that would justify using quadratic or higher-order terms in the magnitude scaling. Most GMMs for free-field ground motions include a site term, but we did not include the site (linear V_{S30} scaling) because there is only weak dependence on V_{S30} in the smartphone data.

We attempt to fit increasingly complex model forms to the data, starting from a simple form with just source (linear magnitude scaling) and geometric spreading terms, only adding more parameters when they result in a tangible reduction in the model standard deviation. Our final model form is inspired by the small-magnitude GMM of Atkinson (2015) and is as follows:

$$\ln(Y_{ij}) = c_0 + c_1 M + c_2 Z_{\text{hyp}} + c_3 \ln(R_{\text{hyp}}), \quad (2)$$

in which Y_{ij} is the MyShake peak acceleration produced by earthquake i at record location j, M is event magnitude, Z_{hyp} is hypocentral depth, R_{hyp} is hypocentral distance, and $c_0 - c_3$ are model coefficients. Our formulation differs from Atkinson (2015) in that it does not make use of the saturation distance h_{eff} to mimic near-field ground-motion saturation, which manifests as curvature and a plateau at near-fault distances in R_{hyp} space due to finite-fault effects (Yenier and Atkinson, 2014). We elect to exclude distance saturation because there is no visual evidence for curvature in R_{hyp} space in Figure 5, and finite-fault effects should be near-negligible for our magnitude range.

We fit our model using the one-stage mixed-effects approach of Abrahamson and Youngs (1992), in which the base model (fixed effects) is fit via maximum-likelihood estimation while allowing a random per-event intercept. This random intercept is conventionally referred to as the event term. Event terms allow for earthquakes that produce below-average or above-average ground motions and can be thought of as the average of the total residuals over all

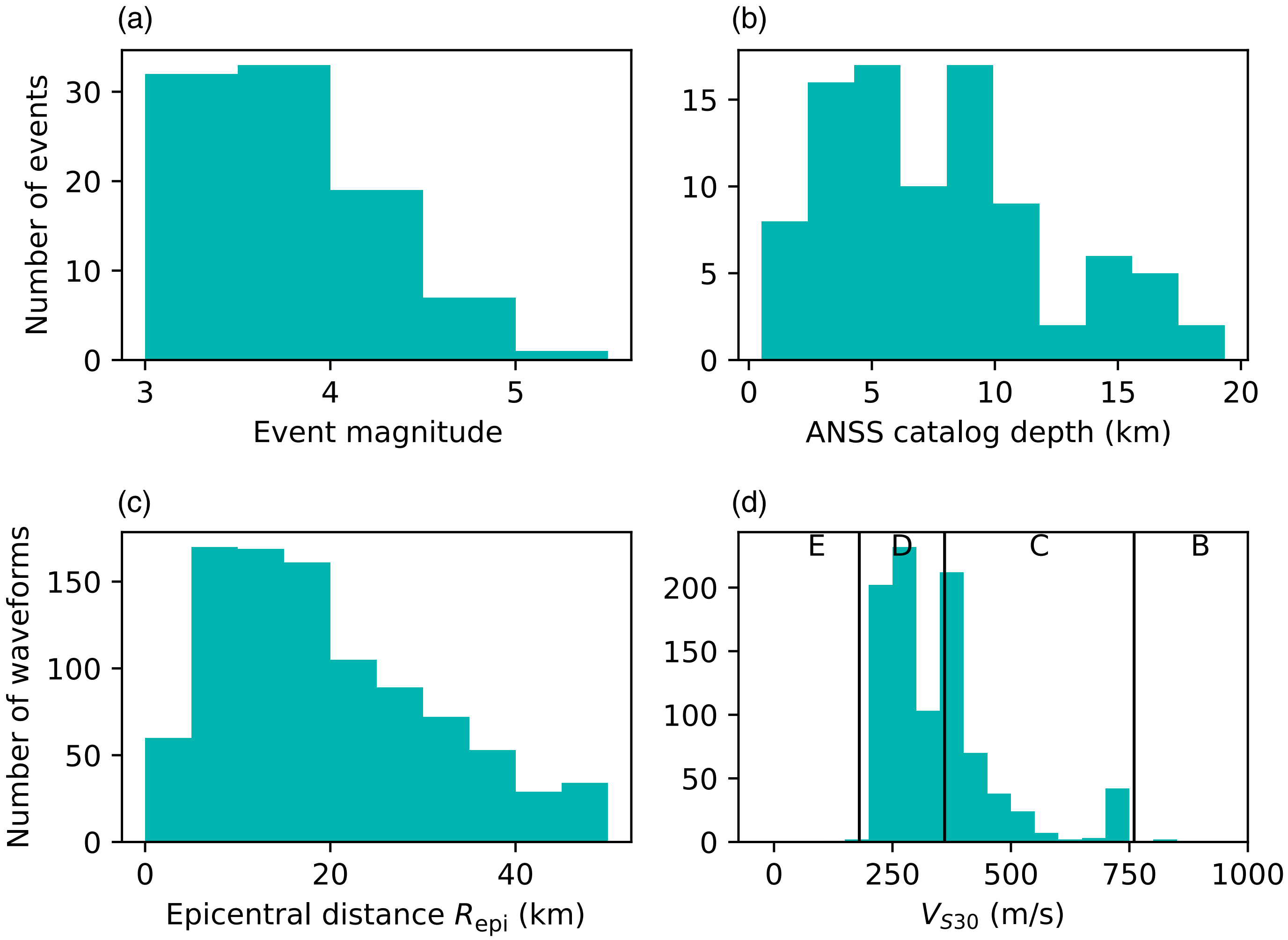

Figure 4. Distributions of predictive event and record variables for the final dataset used in the fitting of MyShake GMM: (a) distribution of event magnitude; (b) distribution of event depth; (c) distribution of record epicentral distance; and (d) distribution of assigned record V_{S30}. Black vertical lines show NEHRP site class boundaries for site classes B–E. The color version of this figure is available only in the electronic edition.

records for one event. The Abrahamson and Youngs (1992) approach allows for event terms to be estimated even for events with just one record. For such poorly sampled events, the residual is partitioned into the event term and the within-event residual based on the ratio of the standard deviations for these two terms, whereas for increasingly well-sampled events, the event term converges to the average of total residuals (Abrahamson and Youngs, 1992; Abrahamson and Silva, 1997). We choose to keep poorly sampled events (with less than three records) to better sample inter-event variability and to prevent only a few events from controlling the magnitude scaling at the $4.0 \le M \le 5.0$ range.

We model each observation using a model of the form

$$\ln(Y_{ij}) = \mu(M_i,R_{ij},\ldots) + \delta B_i + \delta W_{ij}, \qquad (3)$$

in which $\mu(M_i,R_ij,\ldots)$ represents the median model prediction given in equation (2), δB_i is the event term for the ith earthquake, and δW_{ij} is the remaining (within-event) residual, following the notation of Atik *et al.* (2010). The method assumes that δB and δW are independently and normally distributed with standard deviations τ (between-event standard deviation) and ϕ (within-event standard deviation), respectively.

The final fitted model takes the form

$$\ln(Y_{ij}) = -4.116 + 1.201M + 0.072Z_{\mathrm{hyp}} - 1.627\ln(R_{\mathrm{hyp}}). \qquad (4)$$

MODEL OVERVIEW

The final model is shown in Figure 6 as applied to two well-sampled events in MyShake GMDB: the September 2020 **M** 4.5 El Monte, Los Angeles, earthquake and the December 2022 **M** 3.3 Union City, East Bay Area, earthquake. The figure highlights the excellent visual fit to the data in both cases as well as the utility of applying event term-based corrections.

Model standard deviation and residuals

We quantitatively assess our model's performance against the data by considering model residuals. Plots of between- and

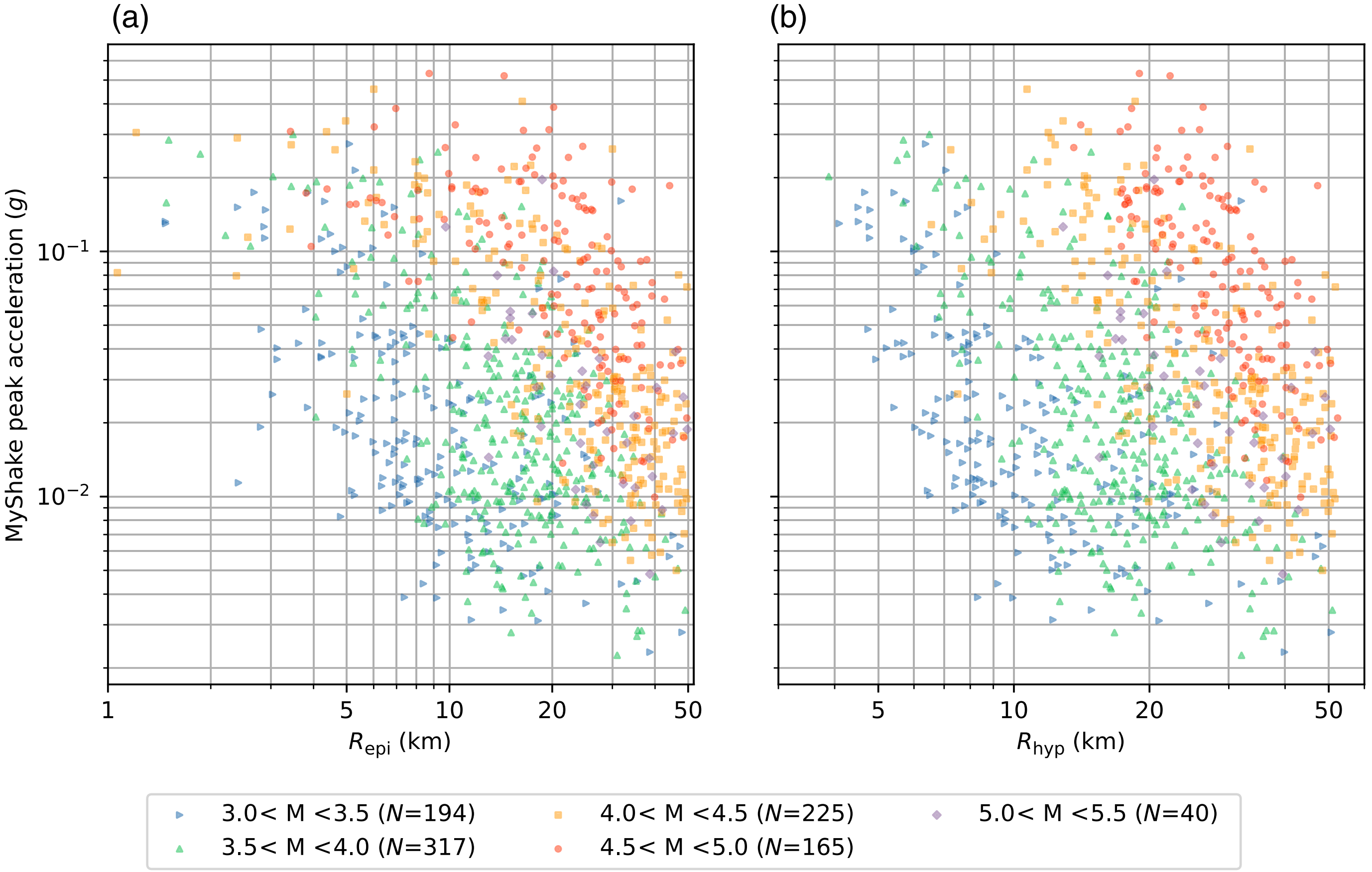

Figure 5. MyShake accelerations for all records in the dataset, (a) against epicentral distance and (b) against hypocentral distance. Data are binned in 0.5 unit magnitude bins, which are distinguished by different symbols and colors. The number of MyShake records in each magnitude bin is given in brackets in the figure legend. The color version of this figure is available only in the electronic edition.

within-event residuals are shown in Figures 7 and 8. We test the model assumptions of normality in the within- and between-event residuals using a Lilliefors test for normality (Lilliefors, 1967). Both sets of residuals pass the Lilliefors test at the 5% level of significance, indicating no statistically significant deviation from normality.

The model standard deviation (σ) is 0.85 natural log units (translating into a spread of 2.3 times about the model median in arithmetic units) partitioned into model between-event standard deviation $\tau = 0.46$ and within-event standard deviation $\phi = 0.71$). By observing plots of the spread in residuals against predictive variables (Figs. 7 and 8), we conclude that there is no evidence to suggest the standard deviation depends on any of our predictive variables. We thus propose a constant standard deviation for our model. The total standard deviation is in line with the σ of 0.75–0.90 natural log units reported for NGA-West2 free-field models for high-frequency SA in **M** 3–4 events (Gregor *et al.*, 2014). Our model's τ is very similar to the τ of 0.4 natural log units reported in the NGA-West2 models, even though we are using a smaller number of events.

Between-event effects. Between-event residuals did not show any trends with respect to magnitude (Fig. 7a), showing our simple source scaling does well for the restricted range of magnitudes used in our model. By contrast, we observed a need to include a depth scaling term. In the initial version of our model that omitted the depth scaling term, we observed an asymmetric distribution of between-event residuals (δB), with event terms trending upward with increasing hypocentral depth (i.e., median amplitudes tended to be higher for deeper events), as shown in Fig. 7c,d. This trend persists for events with event terms constrained by three or more records, in which event terms become more reliable (see Fig. S3). Median high-frequency ground motions have been seen to increase for deeper events, especially at small-to-moderate magnitudes (Boore *et al.*, 2014). This effect has been linked with an increase in stress drop with depth, less strong attenuation in source regions, or a combination of both (Abercrombie *et al.*, 2021). A number of modern free-field GMMs incorporate depth scaling (e.g., ASK14; CB14; CY14). We elected to correct for this effect using a linear depth scaling inspired by the CB14 GMM. This centered the between-event residuals about zero and achieved a 20% reduction in the modeled between-event standard deviation

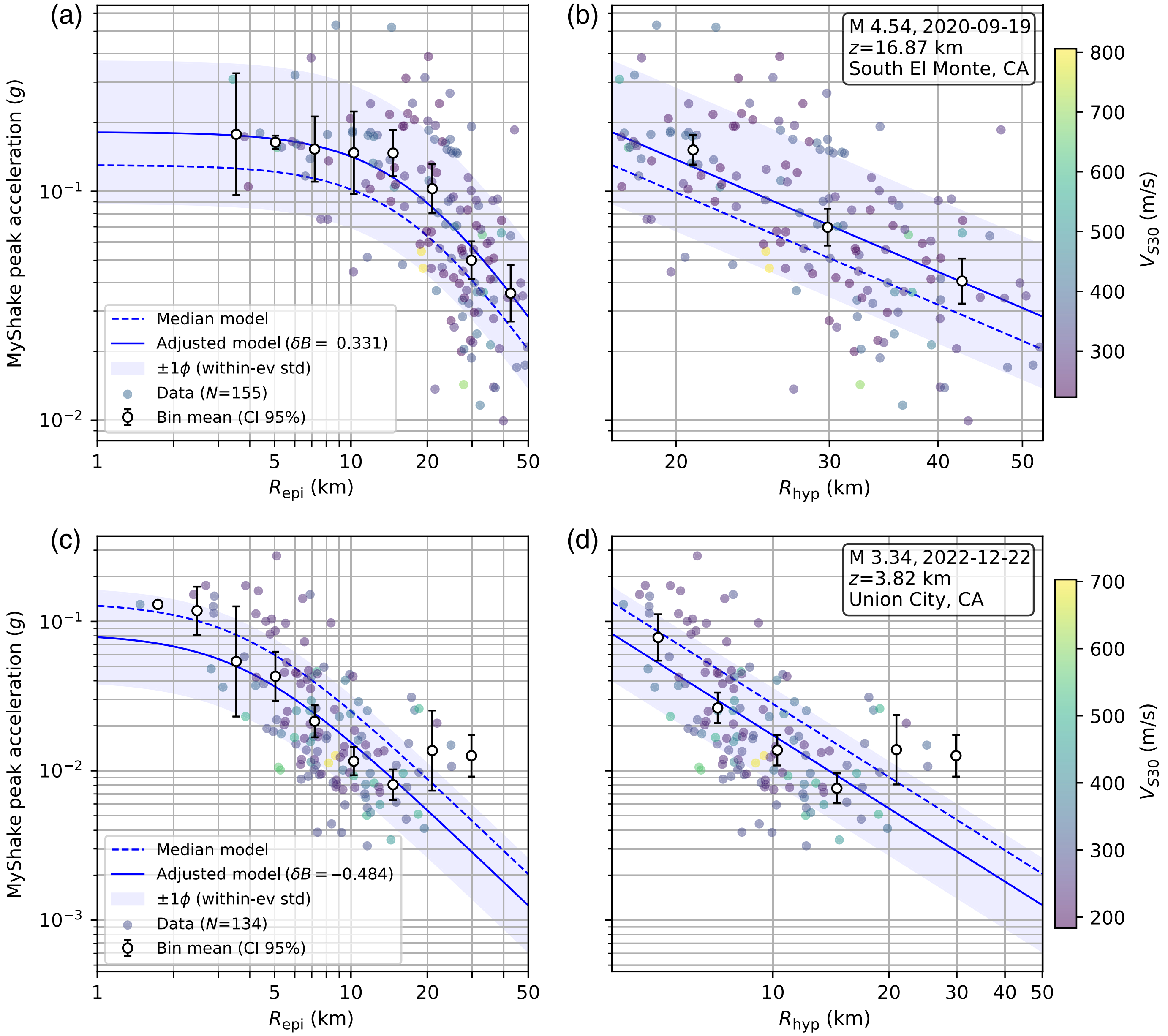

Figure 6. Model predictions and data for (a,b) the September 2020 **M** 4.5 El Monte, Los Angeles, earthquake and (c,d) the December 2022 **M** 3.8 Union City, East Bay Area, earthquake. We show the median model prediction as a dashed line and the event-term-adjusted model prediction as a solid line. Data is plotted as circles, colored by the assigned V_{S30} value. We also show binned means and 95% confidence intervals for the mean. The shaded interval includes the region within one within-event standard deviation (ϕ) of the event-corrected median model. Panels (a) and (c) show the models in epicentral distance space, whereas (b) and (d) show the models in hypocentral distance space. The color version of this figure is available only in the electronic edition.

(τ) from 0.57 to 0.46 natural log units, as seen by comparing Figure 7c and 7e, and 7d and 7f.

Within-event effects. In Figure 8, plotting within-event against R_{epi} and R_{hyp}, we observe no trends with respect to either of these two distance metrics, indicating that our choice of functional form does well to capture median geometric spreading trends in the data. In our final model, the geometric spreading coefficient (c_3) is −1.627 and was the most strongly constrained coefficient in the regression (as it was the coefficient with the smallest relative standard error, see Table S2), in addition to providing a very satisfactory visual fit to the geometric decay of MyShake peak accelerations. Our data justifies using a single rather than a magnitude-dependent c_3 coefficient, with no significant trends in within-event residuals with R_{hyp} across different magnitude bins (Fig. S4). Our c_3 coefficient implies geometric spreading steeper than the R^{-1} decay expected for body waves traveling in a half-space, which would be expected to dominate peak amplitudes in our chosen distance range. However, it is similar to geometric spreading slopes found in the CB14 and CY14 NGA-West2 GMMs for SA at 0.1–0.3 s. It is also extremely similar to the geometric spreading slope obtained for SA at 0.2 and 0.3 s

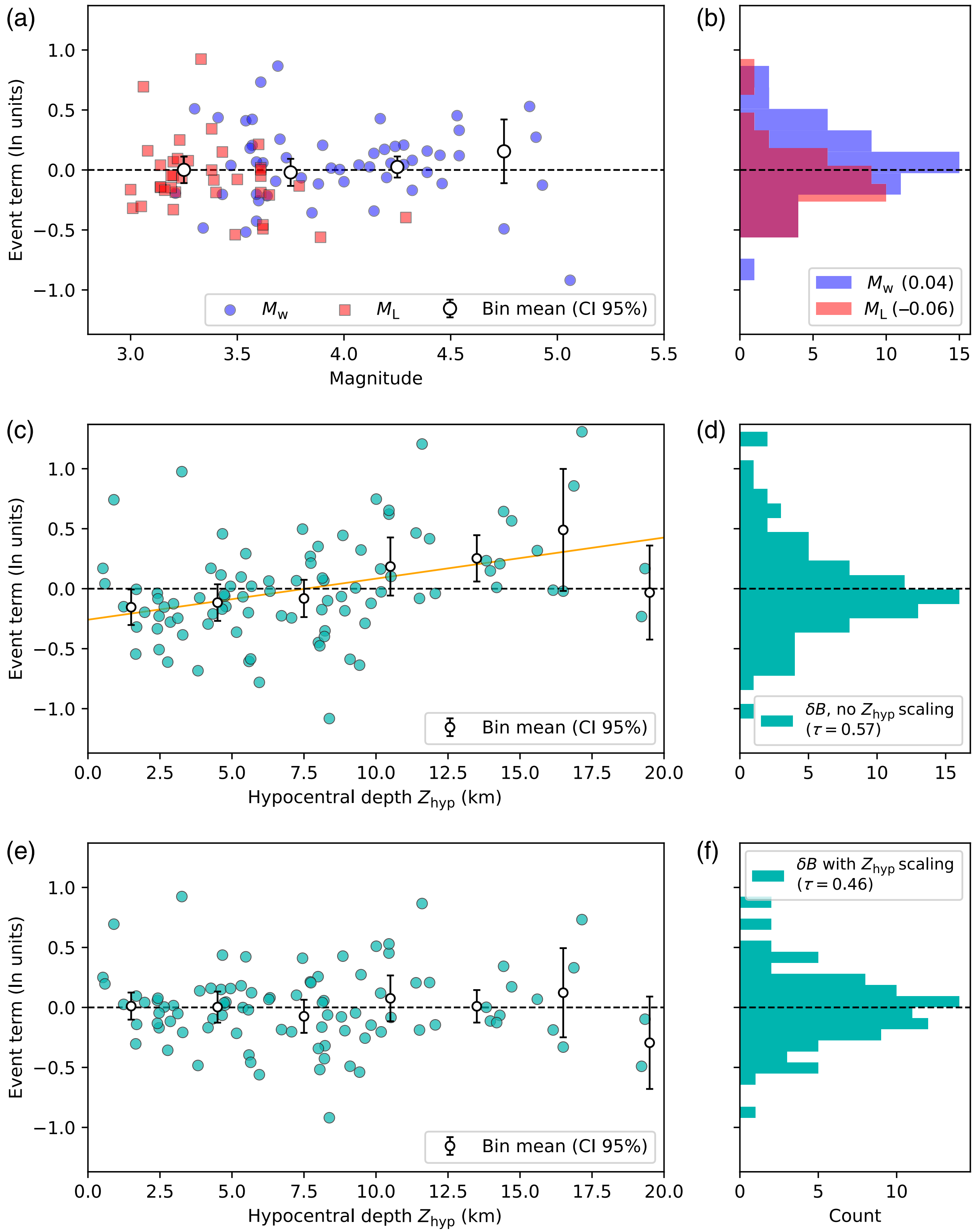

Figure 7. Event term trends against predictive variables. (a) Event term trends against magnitude, separated by magnitude type: moment magnitude (M_w, in blue) and local magnitude (M_L, in red). Binned means for the combined distribution are shown as white filled circles. (b) Event term distribution as a histogram. The mean event term for M_w (blue) and M_L (red) is labeled in the legend. Panels (c)–(f) show event term trends with depth before and after depth scaling adjustment. (c) Scatter plot of event terms without Z_{hyp} scaling. The best-fitting linear trend derived via least-squares fitting is shown as an orange line. Binned means and their standard errors are also shown, as filled white circles with error bars. (d) Histogram of event terms from the model without depth scaling. (e) The same as panel (c), but for the final model including depth scaling. (f) The same as panel (d), but for the final model including depth scaling. The color version of this figure is available only in the electronic edition.

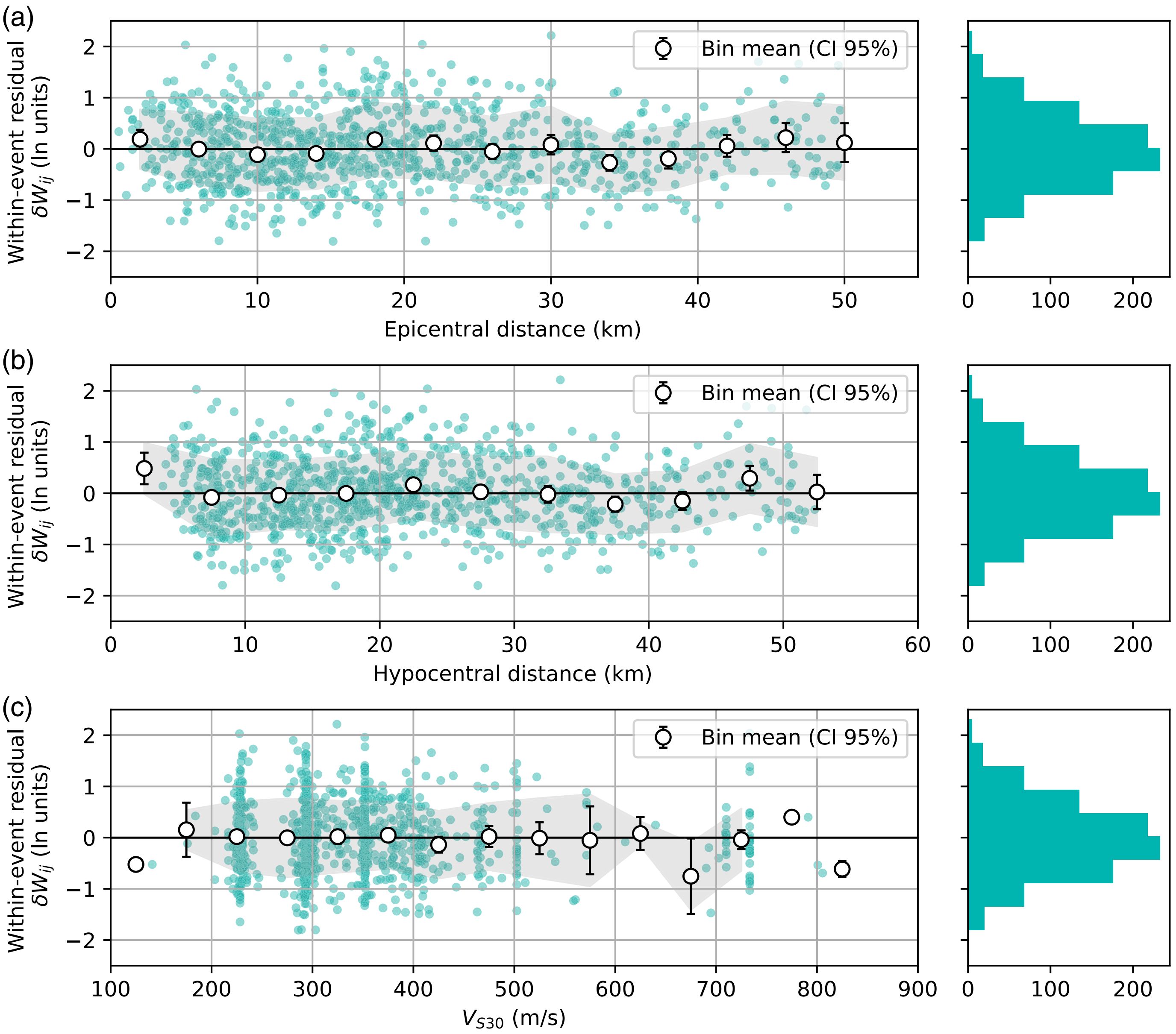

Figure 8. Within-event residuals (δW_{ij}) from the final model, plotted against predictive variables: (a) epicentral distance, (b) hypocentral distance, and (c) time-averaged shear-wave velocity in the top 30 m (V_{S30}). All panels are accompanied by a histogram of within-event residuals. The color version of this figure is available only in the electronic edition.

by Atkinson (2015) in their small-magnitude GMM, which also used R_{hyp} as the distance metric. This offers additional evidence for MyShake data being most strongly influenced by these short periods, owing to its sampling of low-rise residential structures.

In Figure 8, we also observe a lack of a trend of the residuals against V_{S30}. V_{S30} is thought to be a good predictor of site velocity structure (Boore *et al.*, 2011), which should in turn govern site response. It has long been the variable of choice for parametrizing linear site amplification in free-field GMMs. However, a lack of trend of within-event residuals with V_{S30} suggests that MyShake accelerations do not scale with V_{S30}. Fitting an alternative version of our model (see Table S3) that includes a V_{S30}-based linear site term based on Seyhan and Stewart (2014), yields an extremely weak linear site scaling coefficient of −0.100, whereas similarly parametrized free-field GMMs find an equivalent coefficient of around −0.5 to 0.6 for SA at 0.1–0.3 s. It is possible that the extremely narrow range of V_{S30} values in our dataset, as illustrated by Fig. 4c, is not enough to resolve any V_{S30} scaling. We do, however, observe the lack of scaling of MMI within-event residuals with V_{S30} observed by Allen *et al.* (2012) when deriving their Intensity Prediction Equation. Their observation was the strongest for low intensities, using a dataset with a very similar V_{S30} distribution to ours.

Comparison to free-field models

We next compare our MyShake GMM with free-field NGA-West2 models for a number of short-period ground-motion

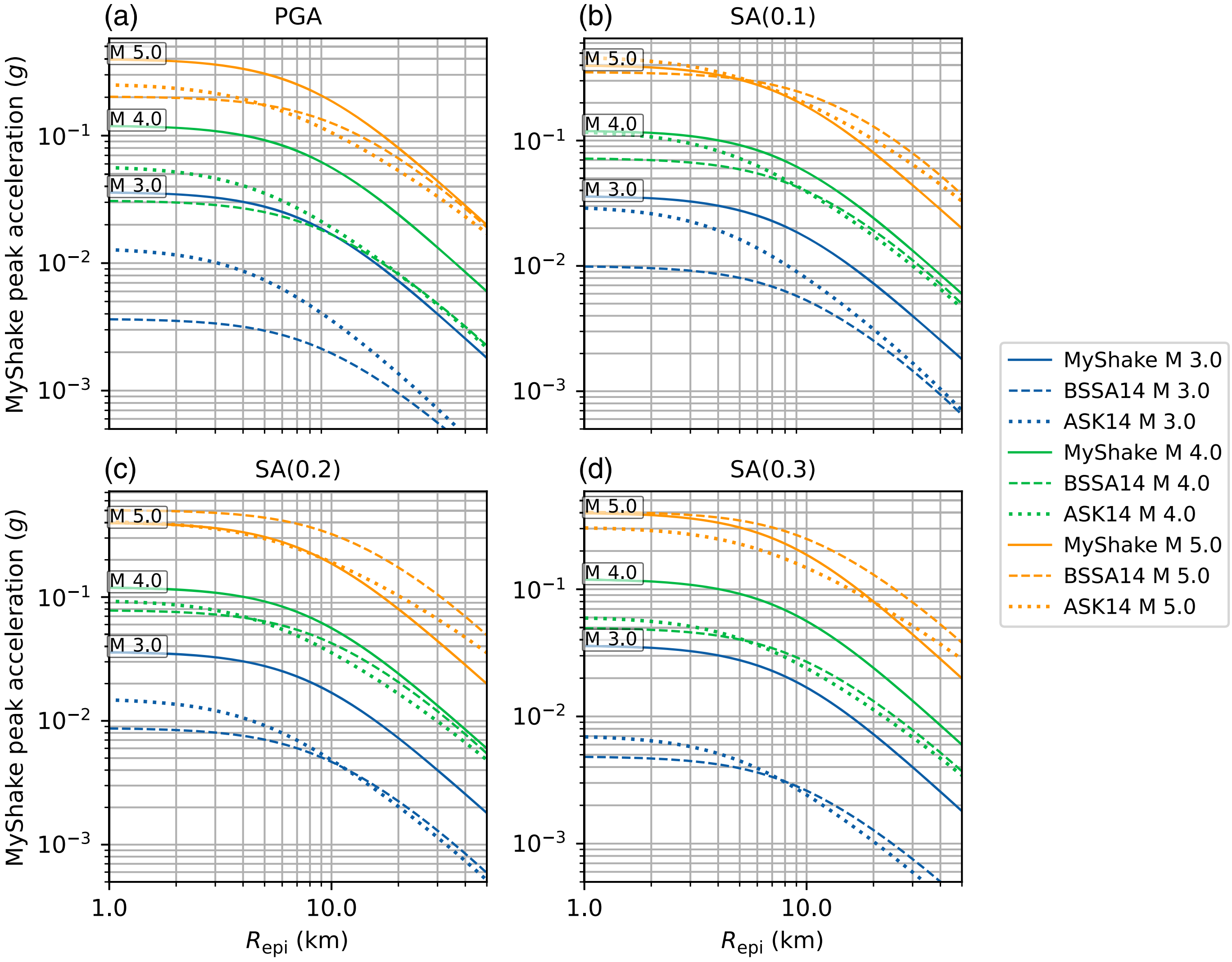

Figure 9. Comparison of the MyShake model against the Abrahamson *et al.* (2014; hereafter, ASK14) and Boore *et al.* (2014; hereafter, BSSA14) NGA-West2 free-field models. We plot the models for four intensity measures (IMs): (a) PGA, (b) spectral acceleration (SA) at 0.1 s, (c) SA at 0.2 s, and (d) SA at 0.3 s, against epicentral distance. We evaluate ASK14, BSSA14, and MyShake GMM for a $V_{S30} = 320$ m/s and a depth of 8 km for **M** 3.0, 4.0, and 5.0. The MyShake model is plotted as a solid line, ASK14 is plotted as a dotted line, whereas BSSA14 is plotted as a dashed line. The color version of this figure is available only in the electronic edition.

metrics to gain a better insight into the factors that affect recorded MyShake accelerations. Figure 9 shows a comparison of MyShake GMM against the ASK14 and BSSA14 NGA-West2 GMMs for PGA and SA at 0.1–0.3 s. We evaluate the free-field models for $V_{S30} = 320$ m/s to match the median V_{S30} of the smartphone dataset, set all basin and style-of-faulting terms to zero, and correct RotD50 predictions to the maximum of two horizontals using the ratios of Boore and Kishida (2016). We also quantified the mean differences in natural log units between the MyShake models and the geometric mean of the two NGA-West2 models evaluated for the four IMs.

We observe that in terms of absolute predicted amplitude, MyShake GMM median predictions are visually the closest to SA at 0.1 and 0.2 s. The mean differences, averaged across magnitudes, are 0.29 and 0.21 natural log units (i.e., the MyShake predictions at SA 0.1 and 0.2 s were 1.34 and 1.23 larger, respectively). The largest absolute differences are observed with respect to the median PGA predictions. When averaged across magnitudes, the MyShake predicted acceleration is 3.0 times (1.11 natural log units) larger than the geometric mean of the two free-field PGA predictions, which is in line with the 3.1 median scale factor for MyShake acceleration with respect to observed PGA reported by Patel and Allen (2022). For SA(0.3 s), the mean difference is 0.63 natural log units (MyShake 1.88 times larger), also in line with Patel and Allen (2022).

The largest differences are observed for magnitude 3.0 (i.e., the smallest earthquakes considered by our model). Across the four IMs, MyShake predictions are on average 4.52 times larger (1.51 natural log units), with the largest differences for PGA, at 7.67 times (2.04 natural log units). We speculate that these large-scale factors might be due to smaller earthquakes containing high-frequency radiation (≥10 Hz), with frequencies matching those of nonstructural elements holding the phones (e.g., desks and tables), causing resonances and significant amplification at high frequencies.

Overall, this comparison exercise with free-field models confirms a recurring observation in this work about how MyShake accelerations are best correlated with the free-field short-period SAs. It also confirms our findings in the Comparison of Smartphone and Free-Field Observations section and those of Patel and Allen (2022). Using median models, which by definition fit the median trends in the data, and averaging differences in logarithmic space across magnitudes, we reproduce the median scale factors of Patel and Allen (2022); yet we also observe a strong magnitude dependence of these scale factors, as we reported earlier in this article. We also observe that the geometrical spreading term in MyShake-GMM is similar to that in the free-field models, as we have previously seen.

CORRELATION OF MYSHAKE AND FREE-FIELD RESIDUALS

Finally, we directly probe the predictive power of MyShake smartphone data for free-field ground motion using the correlation of residuals. The residuals with respect to a predictive model capture repeatable between- and within-event effects, and they can be thought of as having sensitivity to the same features of ground motion when residuals for two distinct intensity metrics are highly correlated. The correlation of residuals from collocated observations of metrics sampling different frequencies (inter-frequency correlation) as well as the correlation of residuals at different locations for metrics at one frequency (spatial correlation) are key aspects of the ground-motion spatial interpolation scheme used in ShakeMap (Worden *et al.*, 2018; Engler *et al.*, 2022). At locations where a desired output metric is not directly observed, it is inferred from an observation of a correlated metric in frequency space (e.g., inferring PGA from an observation of SA at 0.5 s). To produce a spatially continuous grid of ground-motion predictions, ShakeMap uses a spatial cross-correlation model for within-event residuals (Loth and Baker, 2013) to adjust median predictions from a GMM based on ground-motion observations. The spatial correlation of systematic effects is also central to producing next-generation nonergodic GMMs that rely on the variable coefficient model approach to model the spatially variable coefficients and their epistemic uncertainty (e.g., Kuehn and Abrahamson, 2020; Lavrentiadis *et al.*, 2022).

The correlation of total residuals must be assessed in two steps, as the total residual, δ_{ij}, consists of within-event residuals, δ_W, and between-event residuals, δ_B, which are independently distributed and assumed to be uncorrelated (Goda and Hong, 2008). The correlation coefficient, ρ_{tot}, of the total residuals between two intensity metrics, T_1 and T_2 (which could be SAs at two distinct periods, or PGA, PGV) as a function of separation distance, h, is given as

$$\rho_{\mathrm{tot}}(T_1,T_2,h) = \rho_{\delta_B}(T_1,T_2)\frac{\tau_1\tau_2}{\sigma_1\sigma_2} + \rho_{\delta_W}(T_1,T_2,h)\frac{\phi_1\phi_2}{\sigma_1\sigma_2}, \quad (5)$$

in which $\rho_{\delta_B}(T_1,T_2)$ is the correlation coefficient of between-event residuals for the metrics T_1 and T_2, $\rho_{\delta_W}(T_1,T_2,h)$ is the correlation coefficient of within-event residuals for the metrics T_1 and T_2 as a function of the separation distance h, and σ, τ, and ϕ are as previously defined.

In our case, T_1 represents MyShake GMM residuals, and T_2 represents a free-field metric. To run the correlation analysis, we evaluate free-field residuals for SA at 0.1, 1.0, and 3.0 s, as well as PGA and PGV, using observations from ShakeMap against equally weighted predictions from four NGA-West2 active crustal GMMs (ASK14; BSSA14; CB14; CY14), as in the Comparison of Smartphone and Free-Field Observations section. We partition residuals into within- and between-event residuals using a mixed-effects regression. Free-field between-event residuals (event terms) are formed using only the data at $R_{\mathrm{hyp}} \leq 50$ km to avoid mapping any path term misfits into the inferred event terms, as suggested by Baltay *et al.* (2020). Any constant bias terms found by the mixed-effects regression for the free-field event terms are added to the event terms reported by the regression. MyShake residuals are taken from our model regression.

We present scatter plots of MyShake versus free-field event terms, as well as event term correlation coefficients (ρ_{δ_B}), evaluated using the Pearson correlation coefficient, in Figure 10. Even though we did not filter the events for the number of records in our initial regression, we present here only event terms with three or more smartphone records, because these are more reliably constrained (correlations with all events are shown in Fig. S5). We find positive correlations significant at the 5% level for PGA and PGV, with Pearson correlation coefficients of 0.66–0.67. For SA at 0.3 s, the correlation remains significant and stands at 0.58. The lowest correlation is seen for SA at 1.0 s at $\rho_{\delta_B} = 0.50$.

The presence of positive correlations between MyShake and free-field event terms and the reductions when considering longer periods are unsurprising in the light of observations already covered in this article. In our dataset, MyShake records predominantly sample low-rise, short-period fundamental mode buildings. Recorded smartphone accelerations most strongly track high frequencies, which are preferentially excited by small-to-moderate (**M** 3–5) magnitude events with corner frequencies above 1 Hz (1 s) (assuming they follow Brune-type spectra as in fig. 3 of Baltay and Hanks, 2014).

The variation with distance of correlation coefficients between MyShake within-event residuals with those for free-field PGA, PGV, and SA at 0.3, 1.0, and 3.0 s, $\rho_{\delta_W}(h)$, respectively, is shown in Figure 11. We evaluate this correlation by identifying all possible MyShake-free field observation pairs and calculating the Pearson correlation coefficient for data pairs for a range of distance bins. We use a smaller bin width at smaller distances to quantify the short-distance correlation

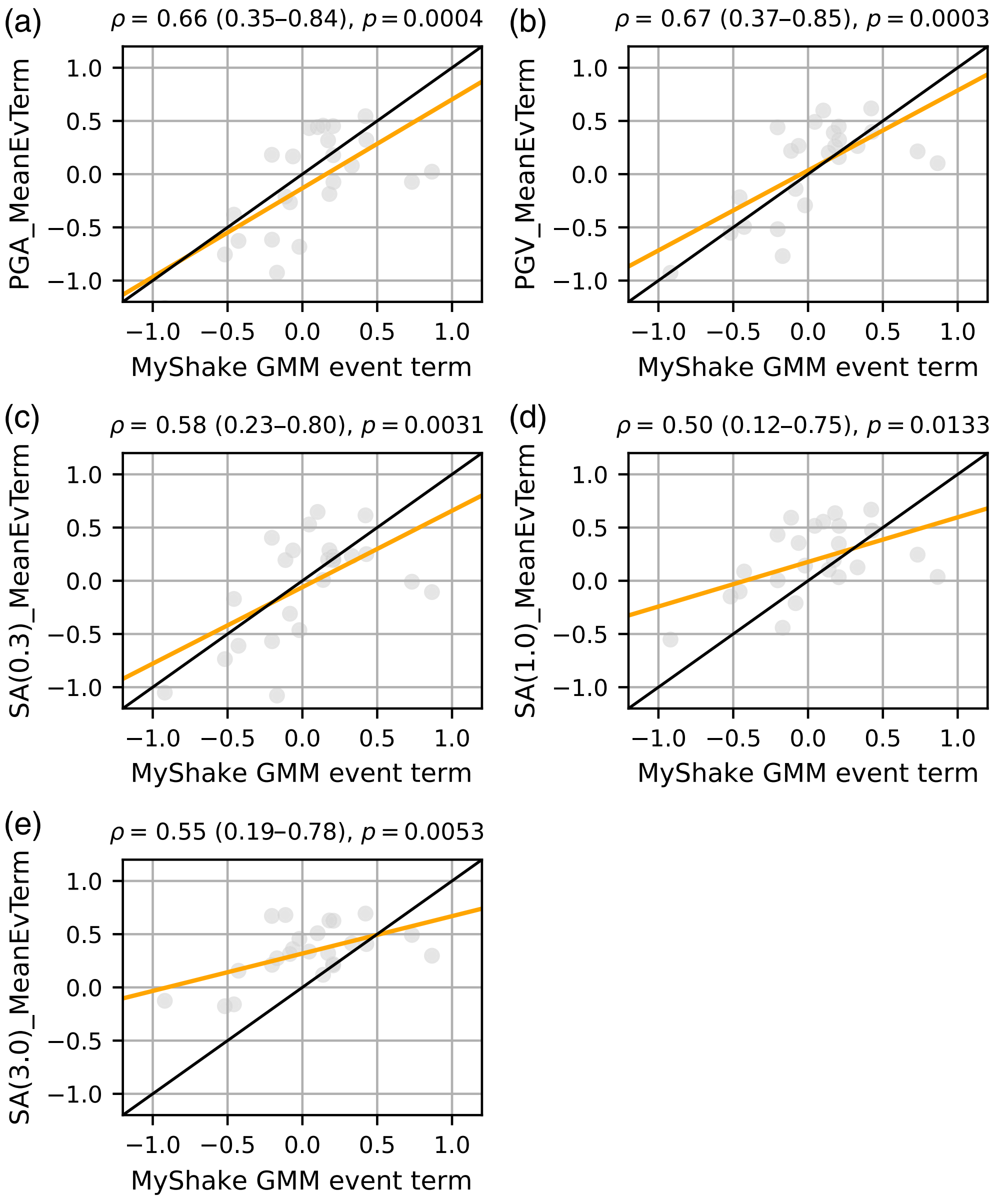

Figure 10. Comparison of MyShake event terms against free-field event terms for five IMs. We only plot event terms that were constrained by three or more records (24 of 92 events). The five panels plot the MyShake event term against the free-field event term: (a) PGA, (b) peak ground velocity (PGV), (c) SA at 0.3 s, (d) SA at 1.0 s, and (e) SA at 3.0 s. In each panel, we also observe the Pearson correlation coefficient for the two datasets, along with bootstrapped 95% confidence intervals and the p-value. The orange lines indicate the best linear fit, whereas the one-to-one line is shown in black. The correlation of event terms for all events, regardless of the number of records, is shown in Figure S5. The color version of this figure is available only in the electronic edition.

more finely. The smallest separation-distance bin of 0–0.5 km contains 25 observations (Fig. 11a). We observe that the correlation predictably falls off with distance, reaching a plateau that is statistically indistinguishable from zero at the 5% level at around 15 km distance (correlations also become nonsignificant at this distance). PGA and PGV show an almost identical correlation, which is higher than for SA(0.3 s). Most significantly, the correlation at very short separation distances (<1 km), which is a proxy for the correlation of collocated MyShake and free-field observations, peaks at 0.38 for SA(0.3 s) and 0.46 for PGA and PGV, indicating good predictive power of MyShake data for these free-field metrics. At these small separation distances, the correlation for SA(1.0 s) and SA(3.0 s) is not significant at the 5% and should not be overinterpreted.

The correlation of MyShake and free-field total residuals, ρ_{tot}, which is expressed as an average of the correlation coefficients of between- and within-event residuals weighted by the standard deviation ratios (equation 5), will be mainly governed by the correlation of the within-event residuals, as $\tau < \phi$ (Carlton and Abrahamson, 2014). The correlation of total residuals at small separation distances is a reasonable proxy for the correlation at zero separation distance (i.e., collocated observations), which in turn is a measure of the predictive power of MyShake data for free-field ground motion. Given that the short-distance correlation between MyShake and free-field PGA, PGV, and SA(0.3 s) δW is around 0.4, we can conclude that the correlation of total residuals is also around 0.4.

SUMMARY AND DISCUSSION

We compile the first-ever consistently processed database of earthquake shaking records from smartphone accelerometers, MyShake-GMDB, using the infrastructure for waveform collection provided by the MyShake app and utilizing the synergy with the USGS ShakeAlert system on the U.S. West Coast. Our database is only an order of magnitude smaller (1619 vs. 20,000) than the gold-standard ground-motion modeling NGA-West2 database for active crustal regions, despite drawing data from 4 yr (2019–2023), as opposed to the almost 80-yr coverage (1933–2011) of NGA-West2. MyShake-GMDB is complementary to

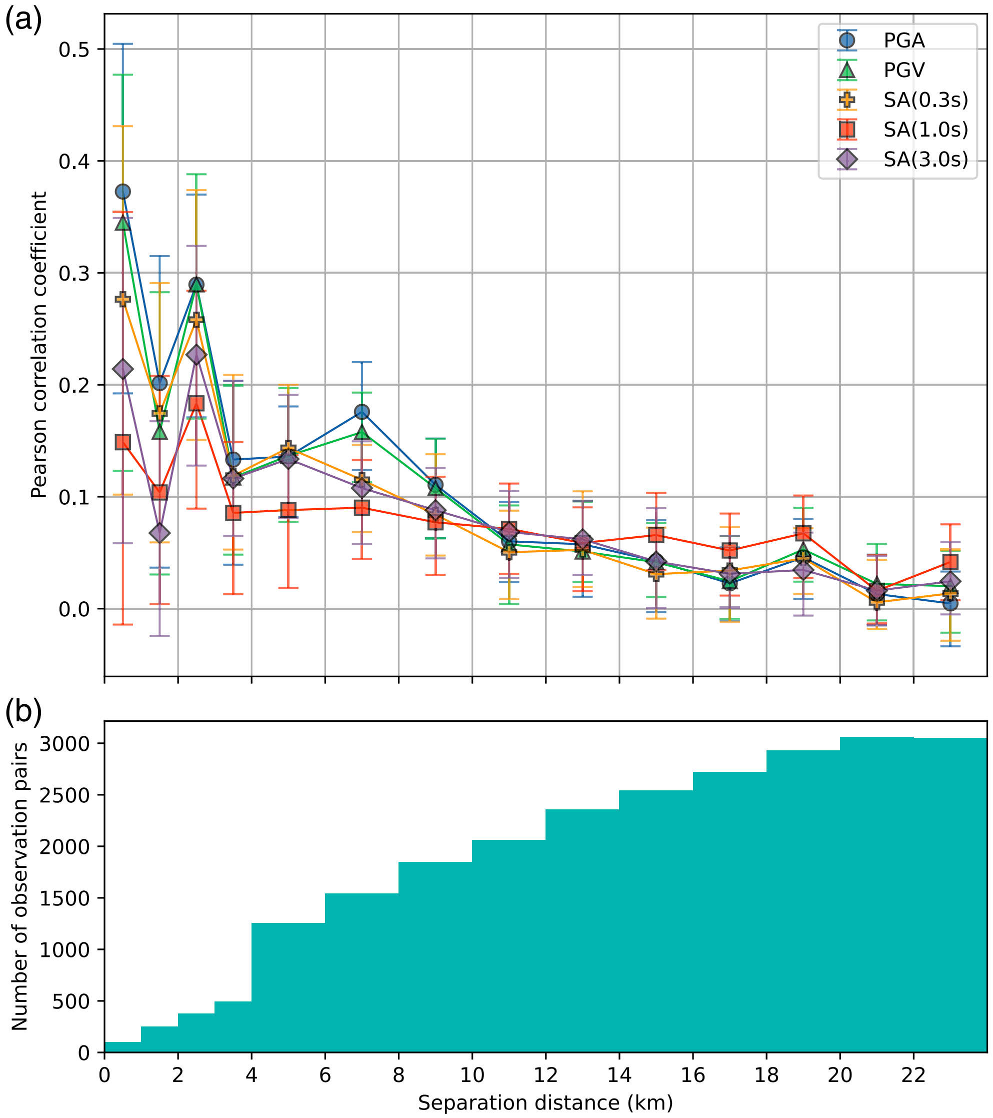

Figure 11. Correlation of MyShake within-event residuals against free-field within-event for PGA, PGV, and SA at 0.3, 1.0, and 3.0 s in different distance bins. (a) Correlation coefficients for the five IMs in different distance bins. For each bin and each IM, we plot the Pearson correlation coefficient with MyShake within-event residuals and bootstrapped 95% confidence intervals as error bars. (b) The number of observation pairs (MyShake paired with free field) for each distance bin used. The color version of this figure is available only in the electronic edition.

NGA-West2 data coverage, providing improved data coverage at short source-to-site distances for small-to-moderate magnitude effects. This could help to address significant epistemic uncertainty in modeling geometric attenuation at small distances for small-magnitude events in current GMMs (e.g., Atkinson, 2015).

We apply ground-motion modeling techniques to this smartphone data to examine its potential utility for modeling the free field, given that smartphone data recorded inside buildings is not free-field data. We first illustrate how MyShake peak accelerations should not be treated as equivalent to free-field PGA, given magnitude- and distance-dependent differences between median predicted amplitudes from free-field GMMs and MyShake data. We develop a GMM for the peak horizontal acceleration recorded by MyShake phones for **M** 3.0–5.5 and $R_{\mathrm{epi}} \le 50$ km using conventional ground-motion modeling techniques, and we use it to further compare MyShake to free-field data.

We find that our median MyShake GMM gives extremely similar geometric attenuation coefficients to those for free-field short-period metrics (SA 0.1–0.3 s). We find this geometric decay to be stronger than canonical R^{-1} decay for body waves. Visual comparison with free-field GMMs further illustrates the comparable geometric attenuation trends. It also illustrates that median MyShake peak accelerations most closely resemble median GMM-predicted SA at 0.1–0.2 s, perhaps highlighting an outsized sampling of one-story structures in MyShake-GMDB.

Our median MyShake GMM shows comparable performance to free-field GMMs in terms of the aleatory variability (model standard deviation), even though MyShake observations carry additional aleatory variability owing to unmodeled building effects, in addition to free-field effects (e.g., source, site, and path effects). Because MyShake-GMDB is rather small compared to the NGA-West2 database, it could be overestimating or underestimating true variability. This can be further investigated by incorporating more data and trying to systematically investigate building effects by incorporating building information (e.g., Sun *et al.*, 2022). Although the required detailed building information is not currently readily available with MyShake records, future versions of the app could provide users with an option to volunteer this information to enable further investigation into the effects of building typology.

Using residual correlation analysis, we show that MyShake data have predictive power for estimating the free-field ground motion. As expected from our GMM comparisons, MyShake within-event residuals, which capture path and site variability, correlate most strongly with short-period metrics, like PGA and SA at 0.3 s. Recovered correlation coefficients for within-event residuals at close (<1 km) stand at 0.4, implying correlation coefficients for total residuals at 0.4. Although this number is based on a rather limited dataset, it lines up well with the 0.4 correlation coefficient between MMI-based felt intensity and PGA or PGV residuals, as reported by Gallahue and Abrahamson (2023). MyShake phones, much like humans reporting their experience of felt intensity, are located mostly within buildings. It is therefore not unreasonable to infer that smartphone-recorded accelerations, viewed through the same building "filter" as felt intensity observations, would exhibit similar dependencies on key ground-motion predictive variables. The lack of a scaling of MyShake peak acceleration with V_{S30}, just like MMI data, as reported by Allen *et al.* (2012), further supports this interpretation. MMI data may not be of the same quality as instrumental ground-motion data, but even as an imperfect predictor of free-field ground motion, they have great value due to the denser sampling compared to seismic stations (Hough, 2000; Quitoriano and Wald, 2020). If dense smartphone data is similarly useful to MMI data as a predictor of free-field ground motion, its addition to ground-motion modeling routines could only prove beneficial.

Using MyShake GMM to form residuals as a means of mapping systematic effects, combined with knowledge of the strength of MyShake data as a predictor of free-field ground motion, opens up avenues for further investigation into the use of MyShake data in many subfields of ground-motion modeling. As the field of ground-motion modeling embraces nonergodic, spatially variable GMM, MyShake data could provide a way to validate estimated nonergodic effects by virtue of sampling particular paths and sites more continuously compared to free-field data. In terms of site response studies, spatially aggregated dense MyShake within-event residuals could be treated using similar approaches to those outlined by Parker and Baltay (2022) for constructing map-based site response models and then used to detect site effects at finer spatial resolution than what can be detected by stations spaced 5–10 km apart. Given the ShakeAlert-MyShake synergy, these data could also be used to validate ShakeAlert ground-motion predictions at a finer resolution. In addition, dense smartphone data could prove useful for the USGS ShakeMap ground-motion geospatial interpolation software. More data is key to ShakeMap ground-motion estimates that better fit observed ground motion and have a lower estimation (statistical) uncertainty (Wald *et al.*, 2022). Attaching an appropriate level of uncertainty to the smartphone data can make for a relatively straightforward incorporation into the ShakeMap multivariate normal interpolation scheme (Quitoriano and Wald, 2020; Engler *et al.*, 2022), providing additional data for conditioning outputs for short-period metrics. In addition, further utilization of MyShake waveforms in conjunction with MyShake's capability to harvest felt reports (Kong *et al.*, 2023) could advance our understanding of the levels of instrumental ground shaking at the location where the user reports their experience of shaking—an advance that has previously been labeled as the "holy grail of human-centric ground-motion seismology" (Quitoriano and Wald, 2020).

Furthermore, in this work we have just used MyShake peak acceleration, whereas we archive full waveforms from MyShake devices. Future work could focus on trying to understand what the MyShake waveform could contribute, both in terms of other peak metrics (e.g., peak MyShake velocity), duration metrics, and frequency-domain metrics. Frequency-domain metrics could provide a more direct link to current GMM practice for engineering applications, which favors modeling the Fourier amplitude spectrum and converting to SA rather than directly modeling SA. Furthermore, frequency domain studies could allow us to spatially probe the relative importance of building versus free-field site effects via the identification of any spatially repeatable resonant peaks in waveforms, as well as better understand frequencies affecting human experience of ground motion (e.g., Sokolov and Chernov, 1998).

Operationally, there are a number of avenues to pursue to maximize the benefit of MyShake data to ground-motion modeling routines. The addition of more data in the magnitude–distance ranges covered by the current MyShake-GMDB would help make MyShake-GMM more robust and could potentially allow for the development of a nonergodic smartphone-based model. Software improvements on the app side could also increase the number of waveforms harvested in instances in which MyShake pushes massive numbers of alert messages from ShakeAlert to the public. Near-source, large-magnitude smartphone data have proven elusive thus far, and the ability of smartphones to capture very high-intensity ground motion remains to be seen, given the potential for clipping (Patel *et al.*, 2023). However, leveraging both advances in automated ground-motion processing software, like the USGS gmprocess software (Thompson *et al.*, 2024), and machine learning techniques, a pipeline can be developed that screens for data quality with less need for manual input. This could enable the regular piping of smartphone data into near-real-time systems such as ShakeMap. It could also enable the streaming of smartphone data into large GMDBs to facilitate investigating systematic effects captured by dense smartphone recordings.

DATA AND RESOURCES

We compiled event data by querying the Advanced National Seismic System (ANSS) Comprehensive Earthquake Catalog (ComCat) available at https://earthquake.usgs.gov/data/comcat/ (last accessed February 2023), using the Python package libcomcat (Hearne and Schovanec, 2022). Next Generation Attenuation-West2 (NGA-West2) ground-motion models (GMMs) were implemented in Python using the OpenQuake engine (Pagani *et al.*, 2014). Model fitting was performed using the lme4 R package (Bates *et al.*, 2015), implemented via the Python package pymer4 (Jolly, 2018). Smartphone waveforms were processed in part using the ObsPy

Python package (Krischer *et al.*, 2015). Figures were compiled using the Matplotlib (Hunter, 2007) and CartoPy (Met Office, 2015) packages in Python. Maps use free vector and raster map data available at naturalearthdata.com (last accessed August 2024), as well as topographic data from the General Bathymetric Chart of the Oceans (GEBCO; GEBCO Compilation Group, 2024). The supplemental material includes five supplemental figures and three supplemental tables. Figure S1 shows trends of total residuals of MyShake and free-field data with respect to predictions from free-field models for spectral acceleration (SA) at 0.3 s. Figure S2 shows the number of unique records per event used in deriving MyShake GMM. Figure S3 is similar to Figure 7 but shows plots of event terms for all considered events. Figure S4 shows the relationship between- and within-event residuals of the MyShake GMM with hypocentral distance, binned by magnitude. Figure S5 is similar to Figure 10 but shows correlations of event terms for all events sampled by smartphone waveforms. Table S1 shows the epicentral distance thresholds used to associate smartphone waveforms with cataloged earthquakes. Table S2 shows the model coefficients and estimation errors associated with the final MyShake GMM. Table S3 is similar to Table S2, but instead shows coefficients for an alternative smartphone GMM that includes a linear site scaling term. The MyShake ground-motion database (GMDB) is available as a supplementary dataset via Zenodo (doi: 10.5281/zenodo.13288173). It contains the MyShake ground-motion record flatfile (containing data from 1619 high-quality waveforms harvested from smartphones globally), the associated event table with source information from the U.S. Geological Survey (USGS) ComCat, and a spreadsheet with header definitions. The flatfile contains the extracted MyShake peak accelerations, record locations, computed distance metrics, and the V_{S30} and surface geologic unit at the observation location.

DECLARATION OF COMPETING INTERESTS

The authors acknowledge that there are no conflicts of interest recorded.

ACKNOWLEDGMENTS

The authors are grateful for the contributions and support from current and former MyShake team and Berkeley Seismology Lab members for their assistance and feedback on this work: Stephen Thompson, Stephen Allen, Akie Mejia, Sarina Patel, and Professor Douglas Dreger. The authors thank all the MyShake user citizen scientists for their data contributions. The authors would like to thank Associate Editor John Douglas and two reviewers for their valuable feedback. This work was funded by the California Governor's Office of Emergency Services (Cal OES), Agreement Number A221010272.

REFERENCES

Abercrombie, R. E., D. T. Trugman, P. M. Shearer, X. Chen, J. Zhang, C. N. Pennington, J. L. Hardebeck, T. H. W. Goebel, and C. J. Ruhl (2021). Does earthquake stress drop increase with depth in the crust?, *J. Geophys. Res.* **126,** no. 10, e2021JB022314, doi: 10.1029/2021JB022314.

Abrahamson, N. A., and W. J. Silva (1997). Empirical response spectral attenuation relations for shallow crustal earthquakes, *Seismol. Res. Lett.* **68,** no. 1, 94–127.

Abrahamson, N. A., and R. R. Youngs (1992). A stable algorithm for regression analyses using the random effects model, *Bull. Seismol. Soc. Am.* **82,** no. 1, 505–510.

Abrahamson, N. A., W. J. Silva, and R. Kamai (2014). Summary of the ASK14 ground motion relation for active crustal regions, *Earthq. Spectra* **30,** no. 3, 1025–1055.

Allen, R. V. (1978). Automatic earthquake recognition and timing from single traces, *Bull. Seismol. Soc. Am.* **68,** no. 5, 1521–1532.

Allen, T. I., D. J. Wald, and C. B. Worden (2012). Intensity attenuation for active crustal regions, *J. Seismol.* **16,** no. 3, 409–433.

American Society of Civil Engineers (2021). *Minimum design loads and associated criteria for buildings and other structures*, Number ASCI/SEI 7-22 in ASCI/SEI 7, American Society of Civil Engineers, Reston, Virginia.

Ancheta, T. D., R. B. Darragh, J. P. Stewart, E. Seyhan, W. J. Silva, B. S.-J. Chiou, K. E. Wooddell, R. W. Graves, A. R. Kottke, D. M. Boore, *et al.* (2014). NGA-West2 database, *Earthq. Spectra* **30,** no. 3, 989–1005.

Atik, L. A., N. Abrahamson, J. J. Bommer, F. Scherbaum, F. Cotton, and N. Kuehn (2010). The variability of ground-motion prediction models and its components, *Seismol. Res. Lett.* **81,** no. 5, 794–801.

Atkinson, G. M. (2015). Ground-motion prediction equation for small-to-moderate events at short hypocentral distances, with application to induced-seismicity hazards, *Bull. Seismol. Soc. Am.* **105,** no. 2A, 981–992.

Atkinson, G. M., and D. J. Wald (2007). "Did You Feel It?" Intensity data: A surprisingly good measure of earthquake ground motion, *Seismol. Res. Lett.* **78,** no. 3, 362–368.

Baker, J. W., and C. A. Cornell (2006). Correlation of response spectral values for multicomponent ground motions, *Bull. Seismol. Soc. Am.* **96,** no. 1, 215–227.

Baltay, A. S., and T. C. Hanks (2014). Understanding the magnitude dependence of PGA and PGV in NGA-West 2 data, *Bull. Seismol. Soc. Am.* **104,** no. 6, 2851–2865.

Baltay, A. S., L. S. Abrahams, and T. C. Hanks (2020). When source and path components trade-off in ground-motion prediction equations, *Seismol. Res. Lett.* **91,** no. 4, 2259–2267.

Bates, D., M. Mächler, B. Bolker, and S. Walker (2015). Fitting linear mixed-effects models using lme4, *J. Stat. Softw.* **67,** 1–48.

Boore, D. M., and T. Kishida (2016). Relations between some horizontal-component ground-motion intensity measures used in practice, *Bull. Seismol. Soc. Am.* **107,** no. 1, 334–343.

Boore, D. M., J. P. Stewart, E. Seyhan, and G. M. Atkinson (2014). NGA-West2 equations for predicting PGA, PGV, and 5% damped PSA for shallow crustal earthquakes, *Earthq. Spectra* **30,** no. 3, 1057–1085.

Boore, D. M., E. M. Thompson, and H. Cadet (2011). Regional correlations of VS30 and velocities averaged over depths less than and greater than 30 meters, *Bull. Seismol. Soc. Am.* **101,** no. 6, 3046–3059.

Bozorgnia, Y., N. A. Abrahamson, L. A. Atik, T. D. Ancheta, G. M. Atkinson, J. W. Baker, A. Baltay, D. M. Boore, K. W. Campbell, B. S.-J. Chiou, *et al.* (2014). NGA-West2 research project, *Earthq. Spectra* **30,** no. 3, 973–987.

Campbell, K. W., and Y. Bozorgnia (2014). NGA-West2 ground motion model for the average horizontal components of PGA, PGV, and 5% damped linear acceleration response spectra, *Earthq. Spectra* **30,** no. 3, 1087–1115.

Carlton, B., and N. Abrahamson (2014). Issues and approaches for implementing conditional mean spectra in practice, *Bull. Seismol. Soc. Am.* **104,** no. 1, 503–512.

Chatterjee, A., N. Igonin, and D. T. Trugman (2022). A real-time and data-driven ground-motion prediction framework for earthquake early warning, *Bull. Seismol. Soc. Am.* **113,** no. 2, 676–689.

Chiou, B. S.-J., and R. R. Youngs (2014). Update of the Chiou and Youngs NGA model for the average horizontal component of peak ground motion and response spectra, *Earthq. Spectra* **30,** no. 3, 1117–1153.

Engler, D. T., C. B. Worden, E. M. Thompson, and K. S. Jaiswal (2022). Partitioning ground motion uncertainty when conditioned on station data, *Bull. Seismol. Soc. Am.* **112,** no. 2, 1060–1079.

Finazzi, F. (2016). The Earthquake Network project: Toward a crowdsourced smartphone-based earthquake early warning system, *Bull. Seismol. Soc. Am.* **106,** no. 3, 1088–1099.

Finazzi, F. (2020). The Earthquake Network project: A platform for earthquake early warning, rapid impact assessment, and search and rescue, *Front. Earth Sci.* **8,** 243.

Finazzi, F., R. Bossu, and F. Cotton (2024). Smartphones enabled up to 58 s strong-shaking warning in the M7.8 Türkiye earthquake, *Sci. Rep.* **14,** no. 1, 4878.

Gallahue, M., and N. Abrahamson (2023). New methodology for unbiased ground-motion intensity conversion equations, *Bull. Seismol. Soc. Am.* **113,** no. 3, 1133–1151.

García, D., D. J. Wald, and M. G. Hearne (2012). A global earthquake discrimination scheme to optimize ground-motion prediction equation selection, *Bull. Seismol. Soc. Am.* **102,** no. 1, 185–203.

GEBCO Compilation Group (2024). GEBCO 2024 grid, doi: 10.5285/1c44ce99-0a0d-5f4f-e063-7086abc0ea0f.

Given, D. D., R. M. Allen, A. S. Baltay, P. Bodin, E. S. Cochran, K. Creager, R. M. de Groot, L. S. Gee, E. Hauksson, T. H. Heaton, *et al.* (2018). Revised technical implementation plan for the ShakeAlert system—An earthquake early warning system for the West Coast of the United States, *U.S. Geol. Surv. Open-File Rept. 2018-1155*, U.S. Geological Survey, Reston, VA.

Goda, K., and H. P. Hong (2008). Spatial correlation of peak ground motions and response spectra, *Bull. Seismol. Soc. Am.* **98,** no. 1, 354–365.

Gregor, N., N. A. Abrahamson, G. M. Atkinson, D. M. Boore, Y. Bozorgnia, K. W. Campbell, B. S.-J. Chiou, I. M. Idriss, R. Kamai, E. Seyhan, *et al.* (2014). Comparison of NGA-West2 GMPEs, *Earthq. Spectra* **30,** no. 3, 1179–1197.

Guy, M. R., J. M. Patton, J. Fee, M. Hearne, E. Martinez, D. Ketchum, C. Worden, V. Quitoriano, E. Hunter, G. Smoczyk, *et al.* (2015). National Earthquake Information Center systems overview and integration, *U.S. Geol. Surv. Open-File Rept. 2015-1120*, U.S. Geological Survey, Reston, VA.

Hearne, M., and H. E. Schovanec (2022). USGS LibComCat, doi: 10.5066/P91WN1UQ.

Heath, D. C., D. J. Wald, C. B. Worden, E. M. Thompson, and G. M. Smoczyk (2020). A global hybrid VS30 map with a topographic slope–based default and regional map insets, *Earthq. Spectra* **36,** no. 3, 1570–1584.

Hough, S. E. (2000). On the scientific value of “unscientific” data, *Seismol. Res. Lett.* **71,** no. 5, 483–485.

Hunter, J. D. (2007). Matplotlib: A 2D graphics environment, *Comput. Sci. Eng.* **9,** no. 3, 90–95.

Jolly, E. (2018). Pymer4: Connecting R and Python for linear mixed modeling, *J. Open Source Softw.* **3,** no. 31, 862.

Kohler, M. D., D. E. Smith, J. Andrews, A. I. Chung, R. Hartog, I. Henson, D. D. Given, R. de Groot, and S. Guiwits (2020). Earthquake early warning ShakeAlert 2.0: Public rollout, *Seismol. Res. Lett.* **91,** no. 3, 1763–1775.

Kong, Q., R. M. Allen, S. Allen, T. Bair, A. Meja, S. Patel, J. Strauss, and S. Thompson (2023). Crowdsourcing felt reports using the MyShake smartphone app, *Seismol. Res. Lett.* **94,** no. 5, 2326–2336.

Kong, Q., R. M. Allen, and L. Schreier (2016). MyShake: Initial observations from a global smartphone seismic network, *Geophys. Res. Lett.* **43,** no. 18, 9588–9594.

Kong, Q., R. M. Allen, L. Schreier, and Y.-W. Kwon (2016). MyShake: A smartphone seismic network for earthquake early warning and beyond, *Sci. Adv.* **2,** no. 2, e1501055, doi: 10.1126/sciadv.1501055.

Kong, Q., A. Inbal, R. M. Allen, Q. Lv, and A. Puder (2018). Machine learning aspects of the MyShake global smartphone seismic network, *Seismol. Res. Lett.* **90,** no. 2A, 546–552.

Kong, Q., S. Patel, A. Inbal, and R. M. Allen (2019). Assessing the sensitivity and accuracy of the MyShake smartphone seismic network to detect and characterize earthquakes, *Seismol. Res. Lett.* **90,** no. 5, 1937–1949.

Krischer, L., T. Megies, R. Barsch, M. Beyreuther, T. Lecocq, C. Caudron, and J. Wassermann (2015). ObsPy: A bridge for seismology into the scientific Python ecosystem, *Comput. Sci. Discov.* **8,** no. 1, 014003.

Kuehn, N. M., and N. A. Abrahamson (2020). Spatial correlations of ground motion for non-ergodic seismic hazard analysis, *Earthq. Eng. Struct. Dynam.* **49,** no. 1, 4–23.

Landwehr, N., N. M. Kuehn, T. Scheffer, and N. Abrahamson (2016). A nonergodic ground-motion model for California with spatially varying coefficients, *Bull. Seismol. Soc. Am.* **106,** no. 6, 2574–2583.

Lavrentiadis, G., N. A. Abrahamson, K. M. Nicolas, Y. Bozorgnia, C. A. Goulet, A. Babič, J. Macedo, M. Dolšek, N. Gregor, A. R. Kottke, *et al.* (2022). Overview and introduction to development of non-ergodic earthquake ground-motion models, *Bull. Earthq. Eng.* **21,** 5121–5150.

Lilliefors, H. W. (1967). On the Kolmogorov-Smirnov test for normality with mean and variance unknown, *J. Am. Stat. Assoc.* **62,** no. 318, 399–402.

Loth, C., and J. W. Baker (2013). A spatial cross-correlation model of spectral accelerations at multiple periods, *Earthq. Eng. Struct. Dynam.* **42,** no. 3, 397–417.

McCann, M., and K. Addo (2012). Probabilistic seismic hazard analysis (PSHA) model, *Technical Rept. Engineering Rept. E658*, BCHydro, Bernaby, BC.

Met Office (2015). Cartopy: A cartographic python library with a Matplotlib interface.

Moschetti, M. P., B. T. Aagaard, S. K. Ahdi, J. Altekruse, O. S. Boyd, A. D. Frankel, J. Herrick, M. D. Petersen, P. M. Powers, S. Rezaeian, *et al.* (2024). The 2023 US National Seismic Hazard Model: Ground-motion characterization for the conterminous United States, *Earthq. Spectra* **40,** no. 2, 1158–1190.

Pagani, M., D. Monelli, G. Weatherill, L. Danciu, H. Crowley, V. Silva, P. Henshaw, L. Butler, M. Nastasi, L. Panzeri, *et al.* (2014). OpenQuake engine: An open hazard (and risk) software for the Global Earthquake Model, *Seismol. Res. Lett.* **85,** no. 3, 692–702.

Parker, G. A., and A. S. Baltay (2022). Empirical map-based nonergodic models of site response in the Greater Los Angeles Area, *Bull. Seismol. Soc. Am.* **112,** no. 3, 1607–1629.

Patel, S. C., and R. M. Allen (2022). The MyShake App: User experience of early warning delivery and earthquake shaking, *Seismol. Res. Lett.* **93,** no. 6, 3324–3336.

Patel, S. C., S. Günay, S. Marcou, Y. Gou, U. Kumar, and R. M. Allen (2023). Toward structural health monitoring with the MyShake smartphone network, *Sensors* **23,** no. 21, 8668.

Petersen, M. D., A. M. Shumway, P. M. Powers, E. H. Field, M. P. Moschetti, K. S. Jaiswal, K. R. Milner, S. Rezaeian, A. D. Frankel, A. L. Llenos, *et al.* (2024). The 2023 US 50-State National Seismic Hazard Model: Overview and implications, *Earthq. Spectra* **40,** no. 1, 5–88.

Quitoriano, V., and D. J. Wald (2020). USGS "Did You Feel It?"—Science and lessons from 20 years of citizen science-based microseismology, *Front. Earth Sci.* **8,** 120.

Rosset, P., A. Bent, S. Halchuk, and L. Chouinard (2022). Positive correlation between DYFI intensity data and microzonation site classes for Ottawa, Quebec City, and the Metropolitan Area of Montreal, *Seismol. Res. Lett.* **93,** no. 6, 3468–3480.

Seyhan, E., and J. P. Stewart (2014). Semi-empirical nonlinear site amplification from NGA-West2 data and simulations, *Earthq. Spectra* **30,** no. 3, 1241–1256.

Sokolov, V. Y., and Y. K. Chernov (1998). On the correlation of seismic intensity with Fourier amplitude spectra, *Earthq. Spectra* **14,** no. 4, 679–694.

Strauss, J. A., Q. Kong, S. Pothan, S. Thompson, R. F. Mejia, S. Allen, S. Patel, and R. M. Allen (2020). MyShake citizen seismologists help launch dual-use seismic network in California, *Front. Commun.* **5,** 32.

Sun, H., H. V. Burton, J. P. Stewart, and J. W. Wallace (2022). Development of a generalized cross-building structural response reconstruction model using strong motion data, *J. Struct. Eng.* **148,** no. 6, 04022053.

Sung, C., N. Abrahamson, and M. Lacour (2023). Methodology for including path effects due to 3D velocity structure in nonergodic ground-motion models, *Bull. Seismol. Soc. Am.* **113,** no. 5, 2144–2163.

Thompson, E. M., M. G. Hearne, B. T. Aagaard, J. M. Rekoske, C. B. Worden, M. P. Moschetti, H. E. Hunsinger, G. C. Ferragut, G. A. Parker, J. A. Smith, *et al.* (2024). USGS automated ground motion processing software version 2.

Thompson, E. M., D. J. Wald, and C. B. Worden (2014). A VS30 Map for California with geologic and topographic constraints, *Bull. Seismol. Soc. Am.* **104,** no. 5, 2313–2321.

U.S. Geological Survey and California Geological Survey and Mineral Resources (2020). Quaternary Fault and Fold Database for the United States, available at https://www.usgs.gov/natural-hazards/earthquake-hazards/faults (last accessed August 2024).

Van Noten, K., T. Lecocq, C. Sira, K.-G. Hinzen, and T. Camelbeeck (2017). Path and site effects deduced from merged transfrontier internet macroseismic data of two recent *M*4 earthquakes in northwest Europe using a grid cell approach, *Solid Earth* **8,** no. 2, 453–477.

Wald, D. J., C. B. Worden, E. M. Thompson, and M. Hearne (2022). ShakeMap operations, policies, and procedures, *Earthq. Spectra* **38,** no. 1, 756–777.

Worden, C. B., E. M. Thompson, J. W. Baker, B. A. Bradley, N. Luco, and D. J. Wald (2018). Spatial and spectral interpolation of ground-motion intensity measure observations, *Bull. Seismol. Soc. Am.* **108,** no. 2, 866–875.

Yenier, E., and G. M. Atkinson (2014). Equivalent point-source modeling of moderate-to-large magnitude earthquakes and associated ground-motion saturation effects, *Bull. Seismol. Soc. Am.* **104,** no. 3, 1458–1478.

Manuscript received 26 August 2024